View metadata, citation and similar papers at core.ac.uk

brought to you by CORE

provided by AFTI Scholar (Air Force Institute of Technology)

Air Force Institute of Technology

AFIT Scholar

Theses and Dissertations

Student Graduate Works

3-2006

A Study of Near Field Data Transformed to the Far Field for a Canonical PEC Scatterer

E. Matthew Cady

Follow this and additional works at: https://scholar.afit.edu/etd

 Part of the Electromagnetics and Photonics Commons

Recommended Citation

Cady, E. Matthew, "A Study of Near Field Data Transformed to the Far Field for a Canonical PEC Scatterer" (2006). *Theses and Dissertations*. 3305.
https://scholar.afit.edu/etd/3305

This Thesis is brought to you for free and open access by the Student Graduate Works at AFIT Scholar. It has been accepted for inclusion in Theses and Dissertations by an authorized administrator of AFIT Scholar. For more information, please contact richard.mansfield@afit.edu.

A STUDY OF NEAR FIELD DATA TRANSFORMED TO THE FAR FIELD FOR A CANONICAL PEC SCATTERER

THESIS

E. Matthew Cady

AFIT/GE/ENG/06-11

DEPARTMENT OF THE AIR FORCE
AIR UNIVERSITY

AIR FORCE INSTITUTE OF TECHNOLOGY

Wright-Patterson Air Force Base, Ohio

APPROVED FOR PUBLIC RELEASE; DISTRIBUTION UNLIMITED

The views expressed in this thesis are those of the author and do not reflect the official policy or position of the United States Air Force, Department of Defense, or the United States Government.

AFIT/GE/ENG/06-11

A STUDY OF NEAR FIELD DATA TRANSFORMED TO THE FAR FIELD FOR A CANONICAL PEC SCATTERER

THESIS

Presented to the Faculty

Department of Electrical and Computer Engineering

Graduate School of Engineering and Management

Air Force Institute of Technology

Air University

Air Education and Training Command

In Partial Fulfillment of the Requirements for the

Degree of Master of Science in Electrical Engineering

E. Matthew Cady, BS

March 2006

APPROVED FOR PUBLIC RELEASE; DISTRIBUTION UNLIMITED.

AFIT/GE/ENG/06-11

A STUDY OF NEAR FIELD DATA TRANSFORMED TO THE FAR FIELD FOR A CANONICAL PEC SCATTERER

E. Matthew Cady, BS

Approved:

/ Signed /

_____ _____

Andrew J. Terzuoli, PhD (Chairman) date

/ Signed /

_____ _____

Lt Col James A. Fellows, PhD (Member) date

/ Signed /

_____ _____

Michael J. Havrilla, PhD (Member) date

Abstract

The purpose of this research was to analyze the error associated with the Image Based Near Field to Far Field Transformation (IB NFFFT) for a canonical perfectly electrically conductive (PEC) scatterer. This research compares two groups of data: far field RCS predicted by the IB NFFFT and far field RCS predicted by X-Patch. The IB NFFFT requires a complete set of calibrated monostatic near field scattering data of the object. A detailed description is given of the configuration of the measurement facilities and procedures that were required to obtain the calibrated near field scattering data, as well as the process for implementing the transformation. Additional chamber characterization techniques are also presented. For this research, a 2-foot long aluminum cylinder of 3-inch diameter was used as the canonical scattering body.

To my mother,

whose support and guidance has enabled me to be where I am today

Acknowledgments

First, I would like to express my sincere appreciation to my committee, Dr. Andrew Terzuoli, Dr. Michael Havrilla, and LtCol. James Fellows, for their guidance in this thesis effort. Special thanks go to Dr. Brian Fischer from General Dynamics Advanced Information Systems for his continual help in tackling the daunting technical challenges of this work.

I owe a great debt to my wife for her patience and understanding during the long nights and weekends that were required to finish this research, and for taking such good care of our infant son during these last several months.

Lastly, I would like to thank Almighty God for the opportunity He has given me to work on this thesis and for sustaining me through many difficult times.

E. Matthew Cady

Table of Contents

List of Figures

Figure Page

List of Symbols

AFIT	Air Force Institute of Technology
AFRL	Air Force Research Laboratory
ASC	Aeronautical Systems Center
AUT	antenna under test
bkg	background
cm	centimeters
CNFFFT	Circular NFFFT
dB	decibels
dBm	decibels referenced to 1 milliwatt
dBsm	decibels referenced to 1 square meter
DFT	discrete Fourier transform
FF	far field
FFT	fast Fourier transform
freq	frequency
ft	feet
GD-AIS	General Dynamics Advanced Information Systems
GHz	gigahertz
GPIB	general purpose interface bus
h-pol	horizontal polarization
IB NFFFT	Image-based NFFFT
in	inches
IDFT	inverse DFT
IFFT	inverse FFT
ISAR	inverse synthetic aperture radar
LO	low observables
MHz	megahertz
MoM	method of moments
NF	near field
NFFFT	near field to far field transformation
ns	nanosecond
PC	personal computer
PEC	perfectly electrically conductive
PO	physical optics
RAM	radar absorbent material
RCS	radar cross section
tar	target
v-pol	vertical polarization
WPAFB	Wright-Patterson Air Force Base

A STUDY OF NEAR FIELD DATA TRANSFORMED TO THE FAR FIELD FOR A CANONICAL PEC SCATTERER

I. Introduction

1.1 Background

The single largest factor that distinguishes the United States Air Force from the air forces of other nations is its use of stealth aircraft. A stealth aircraft is defined as an aircraft that uses low observability as a primary means to accomplish its mission. Low observable (LO) aircraft often have stringent electromagnetic signature requirements that they must meet in order to maintain combat ready status. Diagnostic tests must be performed to verify whether an aircraft's electromagnetic signature is within acceptable parameters. The ability to perform these diagnostic tests in an operational environment is crucial to the warfighter. Historically, special facilities were required in order to measure an aircraft's electromagnetic signature. These facilities are expensive, immobile, and few. More recently, the Air Force has been employing special techniques to perform similar measurements without the need for elaborate test facilities. Often, these diagnostics can even be performed inside a hangar or similar structure. However, there are certain errors that are present in this form of measurement that are not present or are negligible in the traditional type of measurement. If these errors can be understood and quantified, the Air Force will have a valuable tool for keeping its fleet of LO aircraft at peak effectiveness.

The radar and LO communities use a quantity known as radar cross section (RCS) to gauge how detectable an aircraft is. RCS is dependent on the aircraft's shape and

materials, as well as the frequency of the threat radar. RCS is also dependent upon the angle at which the radar waves are incident upon the aircraft, and the polarization of those waves. However, RCS is not dependent upon the distance to the threat radar or the output power of the radar. The details of what RCS is and how it is defined will be discussed in more detail in the next chapter. For now, it is important to note that RCS is the only detection parameter that can be controlled by LO engineers and maintenance personnel. Detection is more likely to occur the closer an aircraft is to a threat radar, but the aircraft's mission often necessitates operating the aircraft in close proximity to enemy air defenses. A low RCS reduces the effective detection range of enemy radars. Electronic warfare and other tactics may be used to further reduce the effective range of threat radars, but this is a complex problem that is outside the scope of this thesis.

As stated earlier, the aircraft's geometry and materials determine what its RCS will be at any given frequency, polarization, and aspect angle. The geometry of the aircraft remains fixed for the most part after the aircraft has entered production. Only minor configuration changes can be made once an aircraft program has entered the operational phase. Wings, stabilizers, and other surfaces cannot be moved for obvious reasons, though they may bend due to stresses placed upon them during flight. Control surfaces, due to their intended purpose, must move during flight, and these movements have an effect on the aircraft's RCS. Similarly, doors for landing gear or munitions can have a pronounced effect on a LO aircraft's RCS when they are open. Even when closed, however, the gaps and steps between bay doors and access panels can affect the aircraft's RCS. Materials also have a great impact on detectability. Radar absorbent material (RAM) is applied to various parts of the aircraft skin to further reduce the RCS. Due to

damage or wear, this RAM may need to be repaired or replaced, and access panels are continually removed and replaced. RAM often requires many man-hours of maintenance to keep the aircraft at combat readiness. After maintenance procedures are performed, diagnostic tests must be run to determine whether or not the aircraft meets specifications for RCS. Sending the aircraft to a remote facility to be checked would be time-consuming, expensive, and impractical.

Historically, RCS could only be measured at an outdoor range. This type of facility has a radar and a pedestal upon which a target is mounted. The distance from radar to target must be great enough so that the waves incident upon the target are locally planar. The exact criteria needed to establish this far field (FF) requirement will be discussed fully in the next chapter. A technique called a near field to far field transformation (NFFFT) can be used to extrapolate the target's RCS from near field measurements. Here, near field (NF) refers to a distance away from the aircraft that is not sufficient to be considered far field. In the near field, the waves are not locally planar, but rather they are spherical in nature. These spherical waves will induce surface currents on the skin of the aircraft different from those induced by a plane wave. Therefore, the scattered, or reradiated, electromagnetic field due to these surface currents is different for spherical wave illumination than for plane wave illumination. An NFFFT takes a set of near field measurements of the target and calculates what the far field RCS would be. There are many different methods that can be used to perform this NFFFT. However, in all cases, there is some error between what the actual RCS is and what is predicted by the NFFFT. To maximize the benefits of this type of diagnostic testing, these errors need to be well understood by the LO community.

1.2 Problem Statement

The Air Force has been making near field RCS measurements for RCS diagnostic purposes on Air Force platforms. These have to be related back to desired/required signature levels. The problem is to correlate near field RCS measurements with far field RCS data and understand the errors.

1.3 Research Question

For the most part, the errors involved with performing near field RCS measurements of aircraft are not well understood. This research focuses on taking near field measurements of a long cylinder, comparing these data to far field data from the same target, and comparing the two data sets. A model has been created to quantify the error, where possible, and a thorough analysis is performed to determine what the errors are and why they occur. This thesis also determines the circumstances necessary for a good correlation to exist between the near field RCS and true far field data.

1.4 Investigative Questions

The following questions must be answered if near field measurements alone are to be sufficient to verify that the United States Air Force's LO aircraft are operating within their RCS specifications:

1. Under what circumstances are the predicted signature levels accurate?
2. How accurate is accurate enough?

3. Under what circumstances does the RCS output from the NFFFT not agree with actual far field data?

4. How gracefully does this transition occur?

5. Can near field RCS data at waterline be used to determine far field RCS at higher elevation angles?

6. Can a correction factor be developed and applied to the near field RCS data, producing a better fit with far field RCS data?

1.5 Summary of Current Knowledge

As was mentioned earlier, RCS is the accepted measure of an aircraft's detectability by radar. RCS is a strictly far field quantity, that is, it is only defined in the far field. To be in the far field, a target must satisfy the criterion given by

$$R \geq \frac{2D^2}{\lambda}. \qquad (1)$$

Where R is the range from the radar to the target, D is the maximum dimension of the target, and λ is the wavelength of the radar. Equation 1 is based on a maximum phase variation across the target of 22.5°. Additionally, RCS is defined as

$$\sigma = \lim_{R\to\infty} 4\pi \frac{\left|\vec{E}^s\right|^2}{\left|\vec{E}^i\right|^2}. \qquad (2)$$

That is, it is proportional to the ratio of the squared magnitudes of the backscattered and incident electric fields as range to target approaches infinity. Because of this condition, RCS ranges have historically been very large. Due to this space requirement, most test ranges have been built outside. Measuring RCS outside is undesirable for two primary reasons. First, radio frequency signals other than the radar's signal are likely present, and may interfere with measurements. Second, since the aircraft being measured are often of

a sensitive military nature, placing the aircraft in an outdoor test range may compromise the project's security. For these reasons, alternative approaches have been used to measure RCS, such as by collimating the incident field into a plane wave using a parabolic reflector. This approach can reduce the space required to take RCS measurements, but the maximum size of a target that can be measured is limited by the size of the parabolic reflector.

Because LO aircraft require a substantial amount of maintenance to ensure that their signatures meet specifications, it is desirable that test equipment be portable, so that diagnostic RCS measurements can be taken in a hangar. Since RCS measurements require that the far field criterion be met, either naturally or artificially (such as using a parabolic reflector), true RCS measurements cannot be taken in such an environment. Rather, only near field measurements can be taken. However, if enough near field measurements are taken over a range of frequencies and aspect angles, this data can be processed using a NFFFT to extract the target's RCS.

Near field to far field methods have been in use for some time, both for predicting RCS and for determining far field antenna patterns. Near field measurement systems save time and money compared with conventional systems, and provide all-weather capability. Additionally, the computed far zone fields are as accurate as those measured in a far field range (Balanis, 2005). However, the far field quantities are not obtained in real-time, but must be processed using sophisticated, expensive software. Near field systems must also be carefully calibrated in order to give good results.

It has been shown that the NFFFTs for scattering and antennas share similar development. Usually what works for one also works for the other. In a sense, the

biggest difference between an antenna and a scattering body is the manner in which the currents are placed on each. However, there are concerns that are specific to NFFFT formulation for RCS calculation. According to Falconer (Falconer, 1988), the near field RCS problem is more complex than the near field antenna problem because the target's scattering pattern depends on the physical nature of the target body and on the electromagnetic field that illuminates it. In other words, in scattering problems, the engineer does not usually choose how the currents will be induced on the target as in antenna problems. To further compound the problem, both the illuminating and sensing probes introduce systematic errors into the recorded data.

More recent developments began using radar image formation from near field data to determine RCS. Odendaal and Joubert (Odendaal and Joubert, 1996) discuss this method in detail, which assumes that the target can be described as a collection of point scatterers that all contribute to the total scattered field. Their approach required image formation to determine RCS.

Ivan LaHaie (LaHaie, 2003) presents a technique for RCS prediction. RCS is a far field quantity—that is, it is only defined as range to the target approaches infinity. This technique developed by LaHaie and his group at General Dynamics Advanced Information Systems (GD-AIS, formerly ERIM), however, predicts a target's RCS based on measurements taken very close to the target. The RCS is then determined from these near field measurements using the image-based NFFFT (IB NFFFT).

There are a variety of NFFFTs that use different developments and geometries, but the one thing they all have in common is that they input near field data and from that data extrapolate the far zone fields. Different NFFFTs have varying levels of

performance and computational complexity (which will be discussed in greater detail later). According to LaHaie, the IB NFFFT is the most practical and mature transformation his group has investigated (LaHaie, 2003).

Although the theory behind the IB NFFFT comes from radar and acoustic imaging, the IB NFFFT does not actually require image formation as part of its implementation. This makes it more efficient than transformations that require image formation (LaHaie, 2003). Radar images can still be formed, if desired, by applying conventional FF inverse synthetic aperture radar (ISAR) techniques to the far field output from the NFFFT. The IB NFFFT is also formulated to take monostatic near field measurements, whereas in general, NFFFTs require a set of bistatic scattering measurements. The IB NFFFT's formulation is found in (LaHaie, 2003). Note that the transformation can occur in two dimensions (e.g. azimuth and elevation), which outputs the RCS over an arbitrary aspect angle from near field measurements taken in multiple scan planes. The transformation can also be performed in one dimension, in which case near field measurements are taken in only one plane, and the RCS is determined only in that same plane. LaHaie's article (LaHaie, 2003) contains a comparison of exact RCS to the RCS predicted by the IB NFFFT.

1.6 Methodology

All investigative questions were answered by an analysis of data collected in laboratory experiments by the researcher. Full sets of NF measurements of a long cylinder were collected in the Air Force Institute of Technology (AFIT) microwave laboratory. A computer program was written in Matlab that takes the near field data sets

and performs an NFFFT on them to arrive at RCS values. This RCS data was compared to simulated far field data. Originally, the FF measurements were to be taken in the AFIT RCS laboratory, or another RCS chamber at Wright-Patterson Air Force Base (WPAFB). However, due to laboratory downtime and other factors, the FF data were obtained through simulation using X-Patch. The NF measurements were very time consuming to collect, since data for both polarizations were collected over a wide range of frequencies and aspect angles.

In order to obtain calibrated NF data, chamber characterization had to be performed. Two different chambers were characterized, and finally a process was developed to obtain calibrated NF data from measured quantities. This calibrated data required the development of a substantial amount of computer code to perform the post-processing. Post-processing was required since no capability existed on the equipment to perform this function. Post-processing functions included initial data formatting, windowing in frequency, range gating, and background subtraction calibration. Dual calibration and chamber background characterization efforts were also undertaken to ensure proper data calibration. The NFFFT was implemented in Matlab and applied to the NF data sets to arrive at predicted FF quantities for the scattering body.

1.7 Materials, Equipment, and Support

As mentioned above, the use of AFIT's microwave laboratory and RCS laboratory were required to fill the matrix of test data for the canonical target. The AFIT microwave laboratory was available for use, but the RCS laboratory was in a state of downtime for upgrades. However, X-Patch was available through AFIT's resources, and

was used as an alternative to obtain the far field quantities. Exact times for data collection were scheduled as necessary. The canonical target that was used in this research was borrowed from the AFIT RCS laboratory. In addition to the professional and academic guidance of Dr. Terzuoli and other thesis committee members, the assistance of an AFIT laboratory technician was required to make configuration changes to the hardware in the AFIT microwave laboratory. The technician was available during the time period when measurements were taken. This required support was minimal and on a case-by-case basis; no full-time or part-time assistance was required.

1.8 External Validity and Standards

The expertise of the LO communities at the Aeronautical Systems Center (ASC) and the Air Force Research Laboratory (AFRL), as well as AFIT faculty, were drawn upon to continually evaluate the research from this thesis at major milestones. ASC had the largest amount of input, and stood to benefit the most from the results of this thesis, since this research is primarily relevant to operational air vehicle acceptance testing. ASC's engineering directorate ultimately reviewed the research from this thesis and its findings.

II. Literature Review

2.1 Scope of Literature Review

This chapter reviews the current state of research on RCS prediction using near field measurements. It describes the background and history of RCS measurement, as well as some of the alternatives to taking true far field RCS measurements. The theory behind various developments of NFFFTs and how they can be used to predict the RCS of a scattering body is discussed. A comparative discussion of the benefits and drawbacks of the IB NFFFT is presented. Finally, the difficulty of using NFFFTs to predict an object's RCS over a wide range of aspect angles using near field data collected over a limited range of aspect angles is discussed.

2.2 RCS Measurements

In order to characterize when an aircraft will be detected by radar, it is necessary to measure its RCS. RCS is strictly a far field quantity, that is, it is only defined in the far field. To be in the far field, a target must satisfy the FF criterion given in Equation 1. Because of this condition, RCS ranges have historically been very large. Due to this space requirement, most test ranges have been built outside. Measuring RCS outside is undesirable for two primary reasons. First, radio frequency signals other than the radar's signal are likely present, and may interfere with measurements. Second, since the aircraft being measured are often of a sensitive military nature, placing the aircraft in an outdoor test range may compromise the project's security. For these reasons, alternative approaches have been used to measure RCS, such as collimating the incident field into a plane wave using a parabolic reflector. This approach can reduce the space required to

take RCS measurements, but the maximum size of a target that can be measured is limited by the size of the parabolic reflector.

Since LO aircraft require a substantial amount of maintenance to ensure their signatures meet specifications, it is desirable that test equipment be portable, so that diagnostic RCS measurements can be taken in a hangar or other convenient location. Since RCS measurements require that the far field criterion be met, either naturally or artificially (such as using a parabolic reflector), true RCS measurements cannot be taken in such an environment. Rather, only near field measurements can be taken. However, if enough near field measurements are taken over a range of frequencies and aspect angles, this data can be processed using a NFFFT to extract the target's RCS.

2.3 NFFFT Overview

Near field to far field methods have been in use for some time, both for predicting RCS and for determining far field antenna patterns. Near field measurement systems save time and money compared with conventional systems, and provide all-weather capability. Additionally, the computed far zone fields are as accurate as those measured in a far field range (Balanis, 2005). However, the far field quantities are not obtained in real-time, but must be processed using sophisticated, expensive software. Near field systems must also be carefully calibrated in order to give good results.

The near field measured data include amplitude and phase information taken at points on a plane, a cylinder, or a sphere. Other sampling geometries exist, such as an elliptic cylinder, a parabolic cylinder, or a sphere in conical surface coordinates (Yaghjian, 1986). However, only the planar, cylindrical, or spherical scans offer

mechanically convenient surfaces with simple orthogonal functions. After the near field is sampled in one of these manners, the measured data are transformed to the far field using analytical Fourier transform methods. The complexity of this operation is determined by the scan geometry. Planar is simplest, followed by cylindrical, and spherical is the most complicated. The choice of scan geometry is determined by the geometry of the object (antenna or scatterer) under test, and the aspects over which the far field data are required.

The planar scan system is best suited for high gain antennas, such as planar phased arrays (Balanis, 2005), and is the least complex computationally. The cylindrical scan system can provide far field data over many aspects (all except high and low elevation angles) while still maintaining fairly simple mechanical requirements. Spherical scanning gives the best aspect coverage (for omnidirectional antenna testing, etc.), but the computational requirements are the highest, and the required mechanical and probing equipment are expensive.

To implement NFFFT techniques, first the tangential electric field is measured (magnitude and phase) over regular intervals on a well-defined surface in the near field. The choice of this surface is dependent upon the scan system (planar, cylindrical, or spherical). By the principle of modal expansion, the sampled electric field data are used to determine the amplitude and phase of an angular spectrum of plane, cylindrical, or spherical waves (Balanis, 2005). Expressing the fields in terms of a modal expansion allows the fields to be calculated at any distance from the target. Setting the distance to infinity gives the far field quantity.

2.3.1 Planar Scan Surface

For the case of a planar scan, sampling is typically performed using an *x*-*y* grid. In this case, the Nyquist rate for spatial sampling is $\Delta x = \Delta y = \lambda/2$. The antenna or scatterer is held stationary while the probe is moved to each test point. As the probe is moved relative to the object under test, its angle relative to the object changes. From these different aspects, the probe will have different gains. These differences in gain, as well as polarization, are taken into account using a technique called probe compensation. Probe compensation methods use the Lorentz reciprocity theorem to couple the far-zone fields of the antenna or scatterer to those of the probe (Balanis, 2005).

As was previously mentioned, the primary advantage of the planar scan over cylindrical or spherical scans is its mathematical simplicity. The planar transformation is well suited to using the Fast Fourier Transform (FFT) algorithm, which is computationally very efficient. If the number of data points is 2^n where n is a positive integer (or the number of data points is zero-padded to 2^n), then the full planar transformation can be computed in an amount of time proportional to $(ka)^2 log_2(ka)$, where a is the radius of the smallest circle that encloses the object under test (Balanis, 2005). The primary disadvantage of planar scans is that the calculated far field is only valid over a limited angular span. If the planar scanning surface is of infinite extent, one complete hemisphere of far field can be calculated (Balanis, 2005). In practice, since planar scan surfaces are finite, the calculated far field will be valid over a solid angle less than 2π steradians.

2.3.2 Cylindrical Scan Surface

If the near field is probed using a cylindrical scan, the far field can be computed for all azimuthal angles except those near the cylinder axis. The numerical integrations are still performed using the FFT, so the cylindrical scan exhibits computation times comparable to those of the planar scan. The angular modal expansion in this case, however, is in terms of Hankel functions instead of plane waves. Hankel functions can be more difficult to calculate, especially at higher orders. Maximum angular and vertical sample spacing is determined by the Nyquist rate, and for cylindrical coordinates, these are

$$\Delta\phi = \frac{\lambda}{2(a+\lambda)} \tag{3}$$

and

$$\Delta z = \frac{\lambda}{2}. \tag{4}$$

Here, λ is the wavelength and a is the radius of the smallest cylinder that encloses the test antenna or scattering body.

2.3.3 Spherical Scan Surface

The spherical scan gives the most complete prediction of the far field radiation or scattering pattern. In this case, the maximum spatial sampling is defined by

$$\Delta\theta = \frac{\lambda}{2(a+\lambda)} \tag{5}$$

and

$$\Delta\phi = \frac{\lambda}{2(a+\lambda)}. \qquad (6)$$

Any far zone pattern cut can be computed from a complete near field scan using a spherical scan system. It should be noted that if the probe is always pointed toward the antenna or scatterer, no probe compensation is required if the scan radius is sufficiently large. If the radius is not sufficiently large, however, probe compensation may still be required.

The mechanical complexity of the spherical scan may be prohibitive, but the primary disadvantage of this scan system is the complexity of its mathematical transformation. A large part of the transform cannot be performed using the FFT. Numerical integrations, matrix operations, and simultaneous solution of equations are required to perform the spherical transform (Balanis, 2005). This in effect increases the computational time and difficulty of the transformation significantly over those of the planar and cylindrical scan systems.

2.4 Planar NFFFT Development

As was mentioned earlier, modal expansion is used to formulate the planar NFFFT. Any arbitrary time-harmonic wave can be represented as a superposition of plane waves traveling in different directions, with different amplitudes, but all of the same frequency (Balanis, 2005). The unknowns to be solved for are the amplitudes and the directions of propagation. The relationships between the near-zone E-field measurements and the far-zone fields for planar systems are given as Fourier transforms, according to (Balanis, 2005)

$$\overline{E}(x,y,z) = \frac{1}{4\pi^2} \int_{-\infty}^{\infty} \int_{-\infty}^{\infty} \overline{f}(k_x,k_y) e^{-j\overline{k}\cdot\overline{r}} dk_x dk_y, \qquad (7)$$

where

$$\overline{f}(k_x,k_y) = \hat{x} f_x(k_x,k_y) + \hat{y} f_y(k_x,k_y) + \hat{z} f_z(k_x,k_y) \qquad (8)$$

$$\overline{k} = \hat{x} k_x + \hat{y} k_y + \hat{z} k_z \qquad (9)$$

$$\overline{r} = \hat{x} x + \hat{y} y + \hat{z} z. \qquad (10)$$

Equation 8 represents the plane wave spectrum of the field. The *x* and *y* components of the electric field measured over a planar surface ($z = 0$) from Equation 7 are

$$E_{xa}(x,y,z=0) = \frac{1}{4\pi^2} \int_{-\infty}^{\infty} \int_{-\infty}^{\infty} f_x(k_x,k_y) e^{-j(k_x x + k_y y)} dk_x dk_y \qquad (11)$$

and

$$E_{ya}(x,y,z=0) = \frac{1}{4\pi^2} \int_{-\infty}^{\infty} \int_{-\infty}^{\infty} f_y(k_x,k_y) e^{-j(k_x x + k_y y)} dk_x dk_y. \qquad (12)$$

The *x* and *y* components of the plane wave spectrum are determined in terms of the near-zone electric field from the Fourier transforms of Equations 11 and 12 as given by

$$f_x(k_x,k_y) = \int_{-b/2}^{+b/2} \int_{-a/2}^{+a/2} E_{xa}(x',y',z'=0) e^{+j(k_x x' + k_y y')} dx' dy' \qquad (13)$$

and

$$f_y(k_x,k_y)=\int_{-b/2}^{+b/2}\int_{-a/2}^{+a/2}E_{ya}(x',y',z'=0)e^{+j(k_xx'+k_yy')}dx'dy'. \qquad (14)$$

The far field pattern of the antenna or scatterer, in terms of the plane wave spectrum is

$$\bar{E}(r,\theta,\phi)=j\frac{ke^{-jkr}}{2\pi r}\left[\cos\theta\,\bar{f}(k_xk_y)\right], \qquad (15)$$

or

$$E_\theta(r,\theta,\phi)=j\frac{ke^{-jkr}}{2\pi r}\left(f_x\cos\phi+f_y\sin\phi\right) \qquad (16)$$

and

$$E_\phi(r,\theta,\phi)=j\frac{ke^{-jkr}}{2\pi r}\cos\theta\left(-f_x\sin\phi+f_y\cos\phi\right). \qquad (17)$$

The procedure to determine the far-zone field from near-zone measurements is (Balanis, 2005):

1. Measure the *x* and *y* components of the electric field in the near-zone.
2. Find the plane wave spectrum functions f_x and f_y using Equations 13 and 14.
3. Determine the far-zone electric field using Equation 15, or Equations 16 and 17.

Developments for cylindrical and spherical NFFFTs may be found in Yaghjian's paper (Yaghjian, 1986).

2.5 NFFFT Development for RCS

It has been shown that the NFFFTs for scattering and antennas share similar development. Usually what works for one also works for the other. In a sense, the biggest difference between an antenna and a scattering body is the manner in which the currents are placed on each. However, there are concerns that are specific to NFFFT formulation for RCS calculation. According to Falconer (Falconer, 1988), the near field RCS problem is more complex than the near field antenna problem because the target's scattering pattern depends on the physical nature of the target body and on the electromagnetic field that illuminates it. In other words, in scattering problems, the engineer does not usually choose how the currents will be induced on the target as in antenna problems. To further compound the problem, both the illuminating and sensing probes introduce systematic errors into the recorded data.

Often, RCS development uses an optical model. At frequencies above the resonance region, it is usually safe to approximate the total surface current with the physical optics (PO) model, given by

$$\bar{J}_s \approx 2\hat{n} \times \bar{H}^i, \qquad (18)$$

where $\hat{n}$ is the unit normal to the surface of the scattering body and $\bar{H}^i$ is the incident magnetic field. Under this assumption, the current also vanishes in the regions that are not illuminated by the incident wave. In the resonance region, other currents such as creeping and traveling waves can act to reduce the accuracy of this approximation.

Multiple scattering may also lead to similar inaccuracies in the estimated surface current (Falconer, 1988).

More recent developments began using radar image formation from near field data to determine RCS. Odendaal and Joubert (Odendaal and Joubert, 1996) discuss this method in detail, which assumes that the target can be described as a collection of point scatterers that all contribute to the total scattered field. Their approach required image formation to determine RCS.

2.6 IB NFFFT

Ivan LaHaie (LaHaie, 2003), presents a technique for radar cross-section (RCS) prediction. RCS is a far field quantity—that is, it is only defined as range to the target approaches infinity. This technique developed by LaHaie and his group, GD-AIS, however, predicts a target's RCS based on measurements taken very close to the target. The RCS is then determined from these near field measurements using the IB NFFFT.

Historically, measuring the RCS of some object required a great deal of space. Since RCS is defined as range approaches infinity, measuring this quantity directly means the probe must be far away. Distances that are very large necessitate outdoor measurements, where the weather and background signal levels may present a problem. Ranges such as these also require a great deal of real estate, and the terrain must be chosen carefully to be conducive to RCS measurement. For these reasons, it is often desirable to perform tests indoors. Compact ranges use parabolic reflectors to create waves that are planar in the vicinity of the target, simulating a source or receiver much farther away. However, for large targets, the compact range's parabolic reflector must

also be large, and this can be prohibitively expensive to implement. Taking near field measurements and performing a transformation to arrive at the far zone fields is often the best choice.

There are a variety of NFFFTs that use different developments and geometries, but the one thing they all have in common is that they input near field data and from that data extrapolate the far zone fields. Different NFFFTs have varying levels of performance and computational complexity (which was briefly discussed in section 2.3). According to LaHaie, the IB NFFFT is the most practical and mature his group has investigated (LaHaie, 2003).

Although the theory behind the IB NFFFT comes from radar and acoustic imaging, the IB NFFFT does not actually require image formation as part of its implementation. This makes it more efficient than transformations that require image formation (LaHaie, 2003). Radar images can still be formed, if desired, by applying conventional FF ISAR techniques to the FF output from the NFFFT. The IB NFFFT is also formulated to take monostatic near field measurements, whereas in most developments, NFFFTs require a full set of single-frequency bistatic scattering measurements. The IB NFFFT's formulation is found in LaHaie's paper (LaHaie, 2003). Note that the transformation can occur in two dimensions, which gives the RCS over arbitrary aspect angle from near field measurements taken in multiple scan planes. The transformation can also be performed in one dimension, in which case near field measurements are taken in only one plane, and the RCS is determined only in that same plane. See LaHaie's paper (LaHaie, 2003) for a comparison of exact RCS to the RCS predicted by the IB NFFFT for a few scattering bodies.

2.7 Justification

NFFFTs provide the means to compute the RCS of a target indoors, in a weather- and signal-controlled environment using far less space that conventional means. The IB NFFFT has many advantages over other transformations in that it requires only monostatic near field data as inputs, it is computationally efficient, and it does not require image formation to determine the far-zone fields (although image formation remains an option). It has demonstrated good performance in predicting RCS, at least in the examples given. The formulation is based on a single scattering model, and so its performance begins to break down as the scattered field becomes dominated by multiple interaction effects. However, even in these cases only the locations of the peaks and nulls are incorrect, and LaHaie has given examples of the IB NFFFT giving surprisingly low errors for the RCS sector averages.

This thesis attempts to build on previous work by demonstrating the IB NFFFT's performance for a long aluminum cylinder. The error between the true far field data and the near field data transformed to the far field using the IB NFFFT is quantified for this scatterer. For this research, all near field data will be actual data collected in a laboratory, not simulated data. The far field data used as the baseline is simulated by the researcher using X-Patch, since the AFIT RCS chamber is unavailable during the course of this work. The method used to collect the near field data is presented in detail in the next chapter.

III. Methodology

3.1 Main Objectives

The primary goal of this thesis is to compare true far field scattering data to near field data transformed to the far field. In order to accomplish this goal, a number of smaller main objectives have been identified in the first chapter of this work. To summarize, these main objectives were:

1. Gather near field scattering data for all objects to be tested.
2. Develop a program to perform the IB NFFFT and apply it to all collected near field scattering data.
3. Gather far field scattering data for all objects to be tested.

In the sections that follow in this chapter, the methods used to achieve these main objectives are described in detail.

3.2 Near Field Scattering Measurement Technique

The techniques that were used in this research to measure the near field scattering for all objects to be tested make up a substantial portion of the total effort of this thesis. Early in the research, efforts were made to locate a laboratory that had the capabilities to perform near field scattering measurements. No such facility was found that was readily available. In searching for a chamber to use, the principal constraint was the distance from the horn or other probe antenna to the pedestal. This distance needed to be short enough so that an object roughly two feet wide would fail to meet the far field requirement as defined by Equation 1 in the horizontal direction for the frequencies of

interest, namely 2-18 GHz. Due to the constraints of using the IB NFFFT in a one-dimensional azimuthal scan, the distance from the probe antenna to the center of the pedestal also needed to be great enough so that the target met the far field criterion as defined by Equation 1 in the vertical direction for the same frequencies. Also, the apparatus needed to support monostatic scattering data collection.

For example, in the early stages of this research, a near field chamber managed by the AFRL Sensors Directorate at Hanscom Air Force Base, MA was identified as a prospect. This chamber employs a compact range-style parabolic reflector to collimate a plane wave for illumination of the scatterer. The scattered field is then probed in the near field of the object bistatically. This geometry is supported by some NFFFT developments, but not the IB NFFFT that this thesis studies. Other chambers failed to meet the requirements of this research for similar reasons.

Besides the criteria for geometric configuration of the prospective near field measurement facility, there were other important factors that needed to be considered before attempts could be made to collect near field scattering data. The chamber had to be available for use, and its use had to be relatively free of charge. The best quality chambers that could be considered are also the busiest and therefore the most expensive to use, and were unavailable. Considering these requirements, only two near field chambers were identified as being available for use. The first is managed by AFRL's Radiation and Scattering Compact Antenna Laboratory (RASCAL) and has been used primarily to measure antenna patterns. The second belongs to AFIT and is part of AFIT's microwave laboratory.

3.2.1 RASCAL NF Chamber

The near field chamber belonging to RASCAL, located in the AFRL Sensor's Directorate building (bldg. 620) at WPAFB, was identified fairly early in the research as a good candidate for near field scattering measurements. The chamber had not been configured or characterized previously for scattering measurements, but the quality of the chamber itself showed promise. This chamber was designed to take near field measurements of a test antenna, which would then be transformed to a far field antenna pattern through an antenna-development NFFFT. The internal dimensions of the chamber are roughly 4 ft. wide by 3 ft. deep by 4 ft. tall. The probe antenna points down and is mounted on two horizontal rails that scan the antenna in a planar or plane-polar manner. The antenna-under-test (AUT) sits on the floor of the chamber, oriented such that the main beam points up toward the chamber ceiling. The transmitted signal is measured by a network analyzer, with one port connected to the probe antenna and one port connected to the AUT. A personal computer (PC) controls the whole system and records the data for post-processing. A diagram showing this chamber's geometry is shown in Figure 1. For more information regarding this chamber, contact Dr. Dan Janning of AFRL/SNRR.

As stated earlier, this chamber had never been used to take near field scattering measurements and needed to be modified for this purpose. First, the connection between the network analyzer and the probe antenna needed to be altered. Since in the antenna measurement configuration, the network analyzer measured S_{21}, an amplifier was included in the path. This amplifier was removed from the circuit, and port 1 of the network analyzer was connected directly to the probe antenna through existing cables.

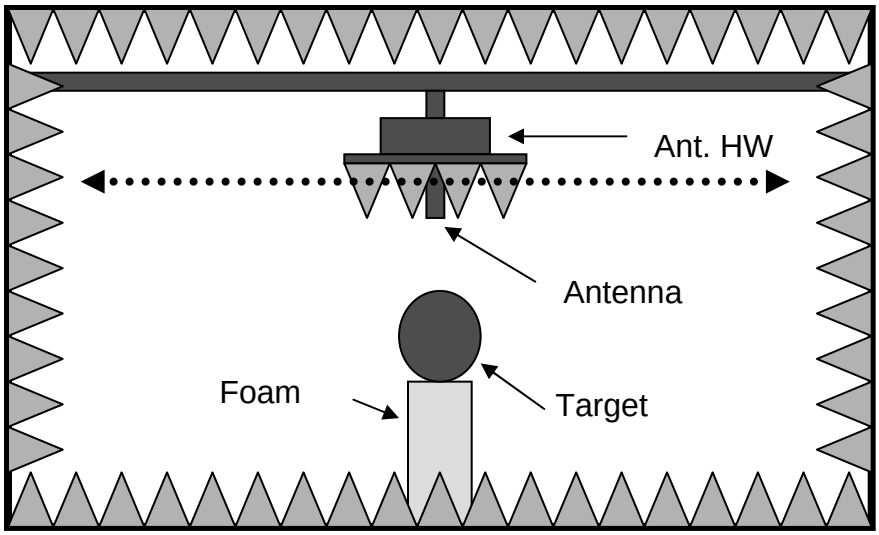

Figure 1. RASCAL NF chamber geometry.

Also, a polystyrene foam column was placed in the chamber to serve as a pedestal for the scattering body. Polystyrene foam is a natural choice of material for this application since its cost is very low and it is nearly transparent at the frequencies of interest (2-18 GHz). Once these modifications were made, the scattering measurements are taken by performing an S_{11} (reflection) measurement on the network analyzer.

Before the chamber is used to take actual near field scattering data, it should first be characterized to ensure that the measurements are good enough for use in the NFFFT. To this end, a 6-inch metal sphere was placed in the chamber on the pedestal and a sample set of measurements was performed. For this experiment, the measurement bandwidth was 4 GHz with a center frequency of 10 GHz. The frequency step size was 10 MHz, yielding a total of 401 frequency samples at each point along the scan line. Spatial sampling was performed along only one of the Cartesian axes (the *x*-axis). Samples were taken along the *x*-axis from -25 to +25 inches, where 0 inches is the center point, the point closest to the scattering body. The sampling was performed every half

inch, for a total of 101 spatial points. According to Yaghjian (Yaghjian, 1986), in order to meet the Nyquist criterion for spatial sampling along the x-direction, the spacing between sample points should not exceed $\lambda/2$. For the maximum frequency of 12 GHz (the shortest wavelength), $\lambda/2$ would be about half an inch. It should be noted that the scan line was about a foot away from the sphere at the closest point, and this is a major source of concern that will be discussed later. Since there were 401 frequency points and 101 spatial points, a reflection matrix can be filled that describes the reflectivity of the object and the chamber at each frequency and point along the x-axis. Note that the object return and the chamber return cannot be separated using this measurement alone.

In order to determine what portion of the reflection measurement is due to the target return, a measurement must also be taken of the target's background. Here, the target's background is defined to be the exact same configuration as the target measurement with the sole exception that the target is not present. Both target and background measurements were performed for the 6-inch sphere, and then the background measurement was subtracted from the target measurement in phase. The time domain result is shown in Figure 2. These results are not yet calibrated, and indicate only magnitude of S_{11}. The time domain quantities were obtained by performing an inverse Fourier transform along the frequency dimension of the scattering matrices. The magnitude of the time domain background measurement by itself is shown in Figure 3. Note that the scale is in decibels (dimensionless) of reflected signal strength. Figure 4 shows both time and frequency domain results for the case where x = 0. The data shown here are before any windowing in frequency or time-gating are applied. Notice that the

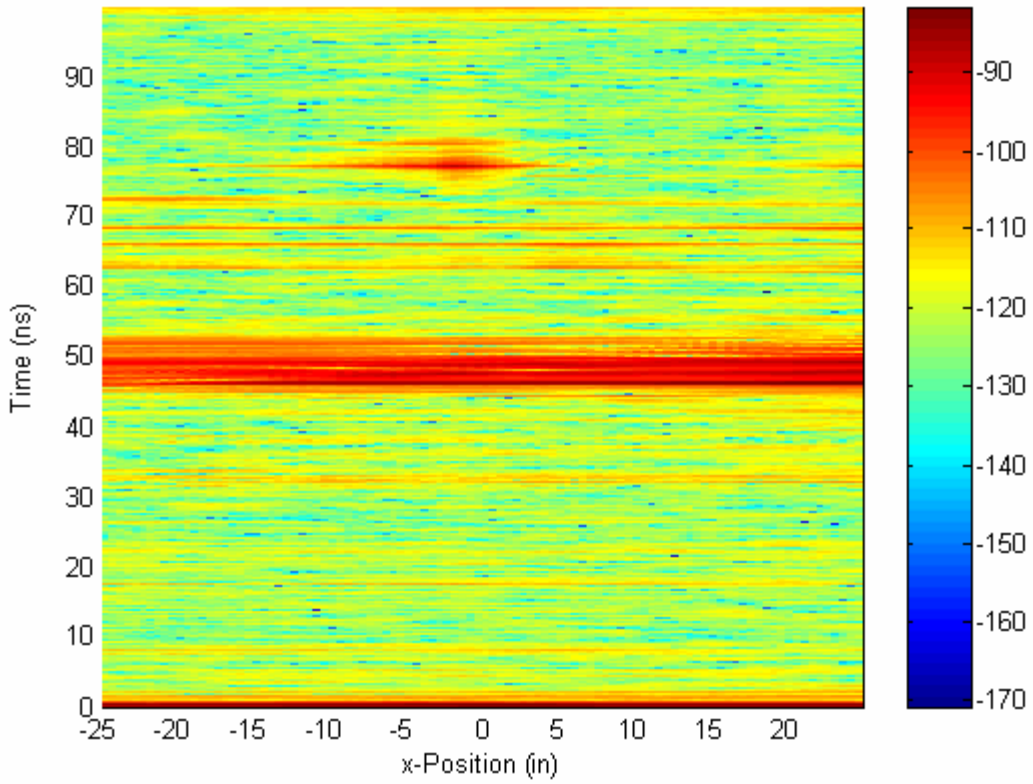

Figure 2. Magnitude of reflection of a 6-inch sphere in the time domain after background subtraction. Note the sphere return localized near 80 ns.

sphere return can be seen in the time domain near 77 ns downrange. Note that the background is 40 – 50 dB higher than the target return itself in these figures. Since the goal of this thesis is to examine the performance of the NFFFT algorithm, it is not desirable to have such high levels of RCS uncertainty in the near field measurements. In an analysis of the NFFFT, this level of uncertainty would mean that it would be impossible to discriminate between errors due to the algorithm and errors inherent in the measurements themselves.

The largest source of concern with this chamber, however, arises from the close

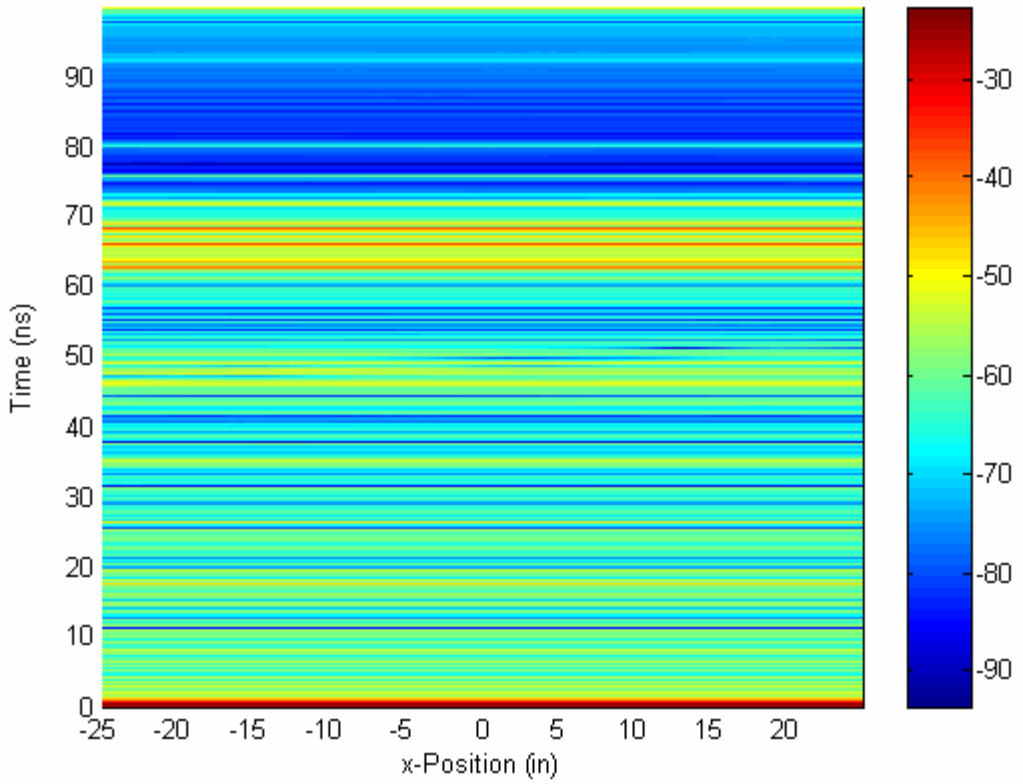

Figure 3. Magnitude of reflection of the background in the time domain with no target present.

proximity of the probe antenna to the scattering body. With about 1 ft. from the tip of the probe antenna to the top of the 6-inch sphere, there is no ability to allow for sufficient settling time on a per-pulse basis to sample the signal. The situation would be much worse for targets larger than a 6-inch sphere, such as the 2-foot cylinder. Under the advice of Dr. Brian Fischer and Dr. Ivan LaHaie of GD-AIS, I decided to abandon any further work to adapt this NF chamber for scattering measurements.

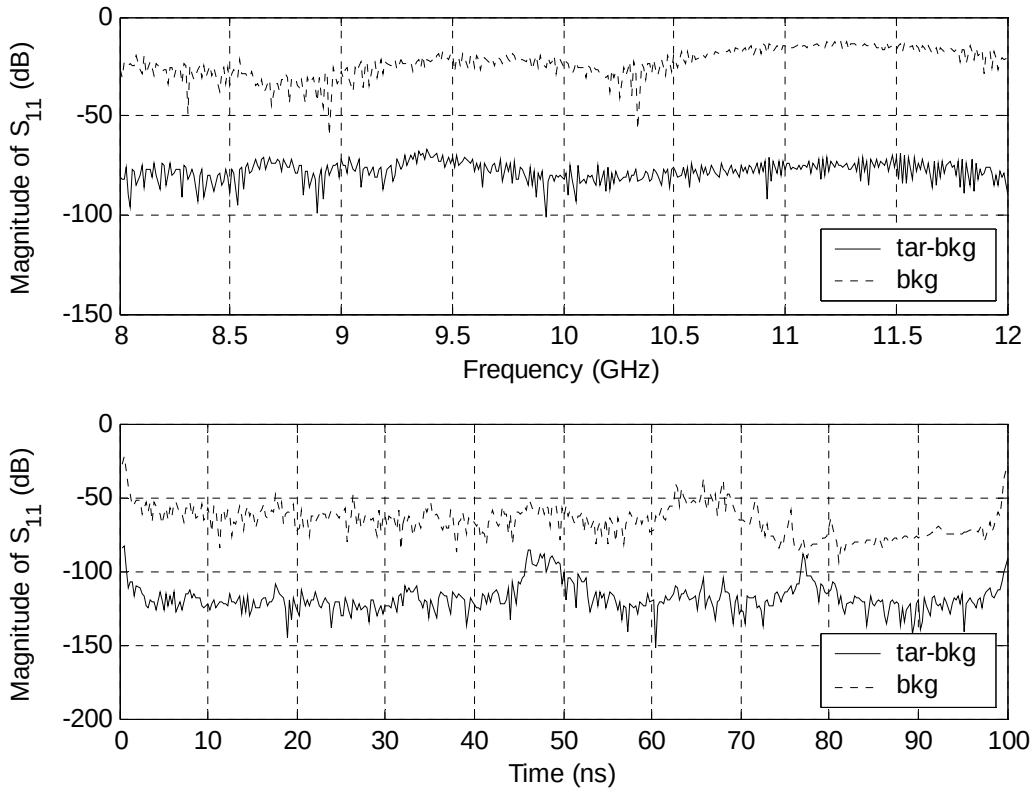

Figure 4. Magnitude of reflection of a 6-inch sphere in the time and frequency domains after background subtraction for x = 0. Magnitude of background reflection is shown on the same axes.

3.2.2 AFIT Microwave Laboratory Chamber

The AFIT microwave laboratory chamber is a instructional-grade anechoic chamber housed at AFIT in building 640. It is made up of a wooden enclosure lined on the inside with foam pyramid and edge absorber. The chamber itself is not externally shielded as most anechoic chambers are, that is, the walls are not lined with metal to prevent external RF signals from interfering with measurements. The pedestal consists of a precision stepping motor with a polystyrene foam column that supports the antenna or scattering body. An HP8510 network analyzer connected to a wideband horn antenna

make up the microwave components of the chamber. The horn is mounted on a circular piece of wood that fits into one wall of the chamber, allowing the horn to be rotated to measure both polarizations. Both the network analyzer and the precision stepping motor are controlled through a general purpose interface bus (GPIB) by a PC running the LabView software package. This chamber had been used primarily for performing antenna pattern measurements.

3.2.2.1 Physical Configuration

In its original state prior to this research, the interior of the chamber was only partially covered by foam absorber. The wooden bracket upon which the horn was mounted was uncovered by any sort of absorbing material. The distance from the horn to the center of the pedestal was about six feet. The foam column that supports the test antenna or scatterer was not tapered at all, but was a wide polystyrene foam cylinder. Figure 5 shows a diagram of the original chamber configuration.

To make the chamber as quiet as possible, and to minimize external interference, spare foam absorber was obtained from the AFIT RCS range at building 168 and added to this chamber. The bare tile walkway was covered by pyramid and edge absorber. Note that the absorbing material had to be moved in order to access the pedestal. While inconvenient, this added measure improved the quality of the measurements. A sheet of foam absorber was also placed behind the horn, reducing the noise in the chamber. In order to minimize the mutual coupling between the pedestal and the scattering body, the polystyrene foam column was cut using a hot tungsten filament so that it was tapered at the top, making it a flat-topped cone rather than a cylinder. Especially at higher

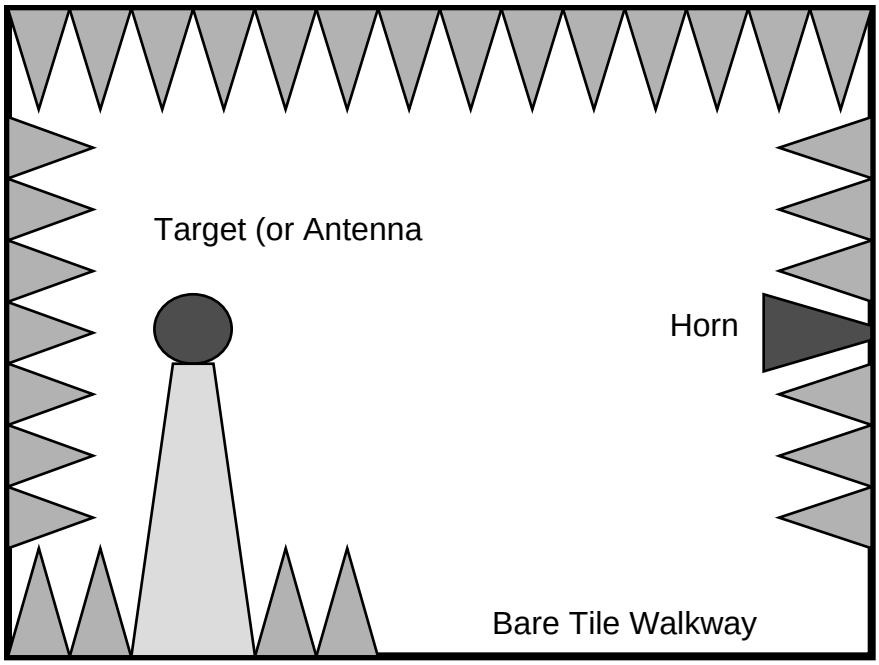

Figure 5. Original chamber configuration of AFIT microwave laboratory anechoic chamber. Original configuration was designed for measuring antenna patterns.

frequencies, polystyrene foam is not perfectly transparent. This precaution minimized the amount of material immediately next to the scattering body during the measurements. Finally, the pedestal itself was moved closer to the horn, such that the distance from the horn to the pedestal center was 191.5 cm (see Figure 6). The motivation for this decision was due primarily to the size of the calibration standards. Unless a near field exact solution for the calibration standards was to be used in order to calibrate the measurements (see the section on calibration methodology below), the distance needed to be such that an object the size of the calibration standard (4.5 – 6 inches) met the far field criterion defined by Equation 1. At the same time, the target to be measured must fail to meet the same criterion in the horizontal direction. Since a measurement bandwidth of 8 GHz with a center frequency of 10 GHz was to be used, the upper limit of the frequency band is 14 GHz. At this frequency and a range of 191.5 cm, the maximum size an object

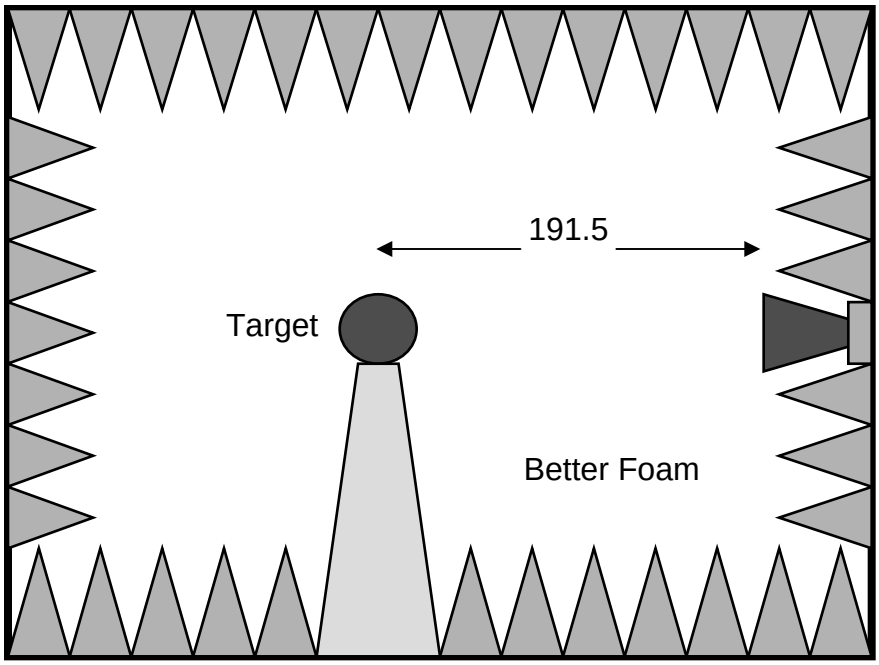

Figure 6. Modified configuration of AFIT microwave laboratory anechoic chamber, redesigned to measure passive scatterers in the near field.

can be and still meet the far field criterion in Equation 1 is about 5.6 inches. For the 6-inch sphere, which is symmetrical about any arbitrary axis that runs through its center, the far field criterion may be relaxed slightly. Therefore, the far field scattering solution may be used for both the sphere and the 4.5-inch squat cylinder calibration standards. A two foot long cylinder would clearly fail to meet the far field criterion at this range and the frequencies of interest. Additionally, the closer the pedestal is to the horn, the stronger the reflected signal. This is because the effective aperture of the horn subtends a larger solid angle, and therefore collects a larger amount of the scattered energy, the closer the pedestal is to the horn. Another added benefit of moving the pedestal closer is in applying a range gate (or time gate) to the data in post-processing. Having the pedestal too close to the back wall limits the size and type of gate function that may be used. It is highly undesirable to have any return from the wall fall inside the range gate. The new

position to which the pedestal has been moved is very close to the center of the chamber, which is ideal for range gating.

3.2.2.2 Software Configuration

The LabView program that controls the chamber measurements was written by Mr. Charles McNeely for performing antenna pattern measurements. A modified copy of this program was created, with some help from Mr. McNeely, to make it suitable for performing scattering measurements. Specifically, the measurement to be taken by the network analyzer had to be changed from S_{21} to S_{11}. Also, the power output needed to be increased to the network analyzer's absolute maximum of +20 dBm on port 1. The sweep time was increased to the maximum of 200 seconds as well. This yields a dwell time of 250 ms for each of 801 frequency points. The dwell time is the time between when the network analyzer reaches phase-lock at the new frequency point and when the returned signal is sampled. The longer dwell time helps to ensure that the chamber is in steady state before the measurement is taken. The longer measurement times caused some time-out errors to occur in the software, and these errors had to be addressed for the system to function properly. These time-out criteria were located in the LabView program and set to values appropriate for this new application, thereby solving the problem.

To help mitigate the noise problems inherent in this chamber, the number of samples at each frequency point that were averaged together to produce the final measurements were increased. Initially averaging only 8 samples, this value was raised to 64, then to 1024, and finally to the maximum allowed by the HP 8510 network

analyzer, 4096 samples. While the higher values for averaging tended to produce better results, they also required more time for the data to be collected. Each azimuth angle of each measurement required a full frequency sweep across the 6 – 14 GHz band. Maximum averaging was causing data collection to take a prohibitive amount of time, and the 15 minutes per frequency sweep that maximum averaging required was deemed too long. To make matters worse, erratic software behavior was causing the system to stop in mid-scan. Most of the data that were used in this research used 1024-sample averaging.

3.2.2.3 Windowing and Time Gating

Before any measurements were put through the background subtraction routine for calibration, they needed to be time gated. This process is sometimes referred to as range gating. The two terms are essentially equivalent, since range and time are related by the speed of light divided by two according to

$$R = \frac{ct}{2}, \tag{19}$$

where R is the range to the target and c is the speed of light in a vacuum. The extra factor of two is added for scattering applications, since the electromagnetic waves must propagate to the target and back to the receiver. It was decided fairly early on to use a Blackman function on the time gate, since unlike many similar functions, the Blackman goes perfectly to zero at its endpoints. This is a desirable property because it totally

rejects all returns that do not fall within the region of time where the target return is expected. Other functions were explored as possibilities, but the Blackman gave the best results. Adding a flat top in the middle of the gate function with unity magnitude has the added benefit of not attenuating any of the returns from the target, as long as the width of the center section is chosen correctly. Since the target for this research was a two foot long cylinder, a center section corresponding to two feet centered on the middle of the pedestal was chosen, with one foot of Blackman roll-off on each end.

Time gating is obviously performed in the time domain. However, the raw measurements are obtained directly in the frequency domain. Therefore, the frequency data must be transformed to the time domain before the gate function can be applied. This is accomplished by an inverse Fourier transform, specifically, an inverse discrete Fourier transform (IDFT). The transform is an inverse because of the chosen time convention ($e^{-j\omega t}$). Note that the inverse FFT (IFFT) algorithm cannot be used in this case. The IDFT must be used instead, because the number of frequency points is not a power of two, but 801. However, the IFFT command in Matlab makes this distinction automatically, and is used throughout this work. Before the data are transformed to the time domain, the data are windowed in the frequency domain.

A window function is similar to a time gate, only it is applied in the frequency domain. For this research, a Hamming window was chosen that spans the entire measurement bandwidth. The Hamming function was chosen for this purpose because it does not go to zero at its endpoints, and so the frequency endpoints still contribute somewhat. Figure 7 shows the final window and gate functions that were used in this research. Windowing has the effect of smoothing the data in the time domain once the

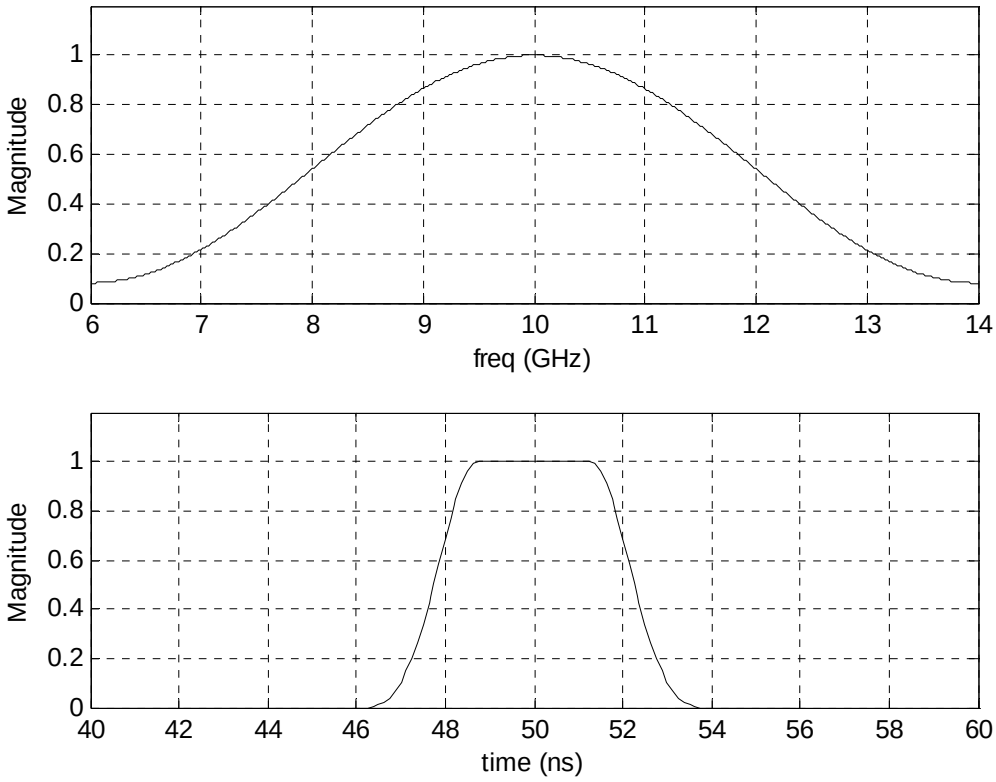

Figure 7. The Hamming window function (top) and the flat-topped Blackman gate function (bottom).

IDFT is performed, and is usually beneficial whenever the data is sampled at discrete points. A variety of window functions were tried, including no window function at all. The Hamming window produced the best results, and so it is used throughout this work.

A good method to test the windowing and time-gating scheme is to run the exact scattering data for the calibration standards through the window-gate combination and then perform a discrete Fourier transform (DFT) back to the frequency domain, and compare the results to the original solution. This was done for both the 6-inch sphere and the 4.5-inch squat cylinder. The results are shown in Figures 8 and 9. The windowed and gated exact solutions in both cases track the unaltered exact solutions very well. The

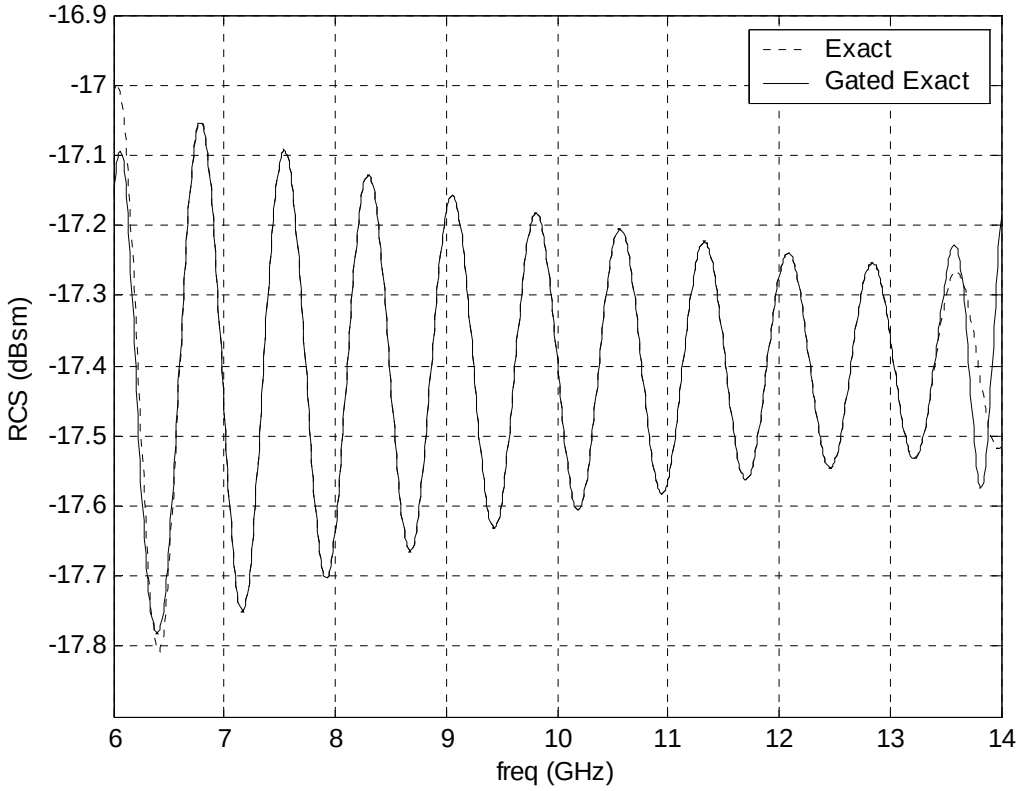

Figure 8. The exact RCS of a 6-inch sphere before and after the window and gate functions are applied.

only significant deviation is observed near the frequency endpoints. However, this is due more to the IDFT/DFT pair and the fact that there are a finite number of samples than to the window and gate functions themselves.

3.2.2.4 Background Subtraction Calibration

A technique known as background subtraction simultaneously separates target return from other chamber returns and calibrates the scattering matrix elements to a known quantity, such as meters. For instance, if A is an element of the calibrated

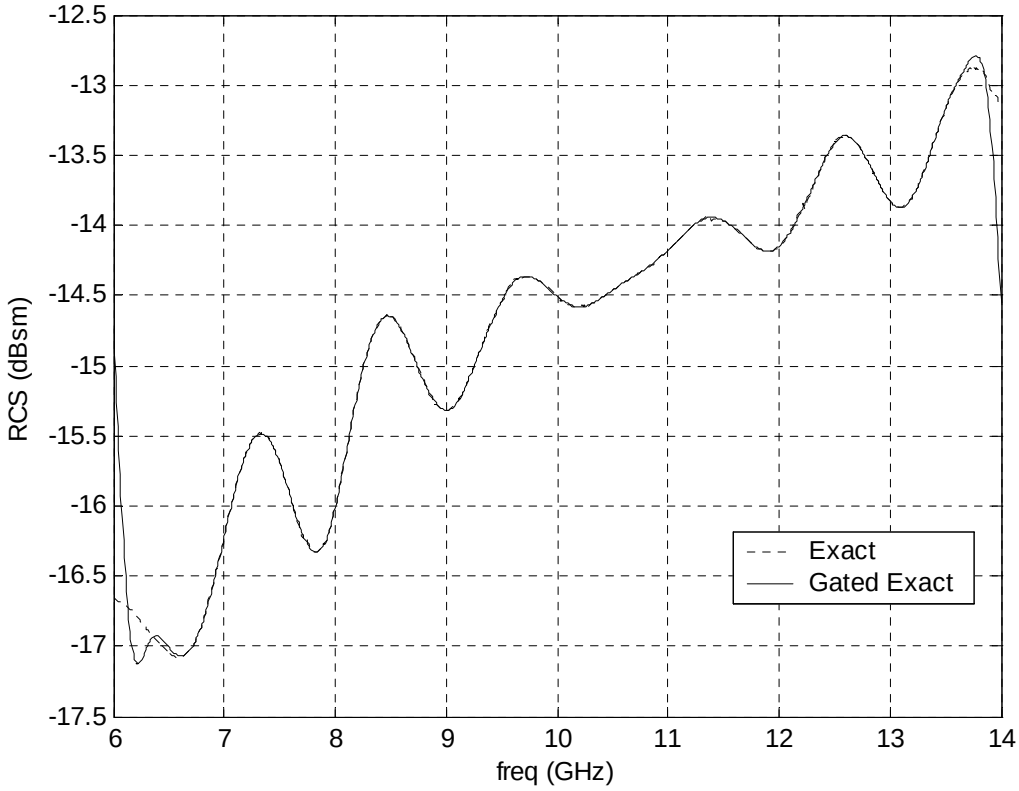

Figure 9. The exact RCS of a 4.5-inch squat cylinder, vertical polarization, before and after the window and gate functions are applied.

scattering matrix, $20\log_{10}|A|$ then has units of dBsm, or decibels relative to a square meter. This background subtraction is defined by

$$IQ_{calibrated} = \frac{IQ_{tar} - IQ_{bkg}}{IQ_{cal} - IQ_{cbk}} IQ_{exact}, \qquad (20)$$

where

$$
\begin{aligned}
IQ_{tar} &= S_{11}\ measurement\ of\ target \\
IQ_{bkg} &= S_{11}\ measurement\ of\ target's\ background \\
IQ_{cal} &= S_{11}\ measurement\ of\ calibration\ target \\
IQ_{cbk} &= S_{11}\ measurement\ of\ calibration\ target's\ background \\
IQ_{exact} &= exact\ solution\ for\ calibration\ target \\
\sigma_{NF} &= 20\log_{10}\left|IQ_{calibrated}\right|.
\end{aligned}
$$

The *IQ* notation is used to indicate that these quantities are complex. Magnitude and phase information are contained in I (in-phase) and Q (quadrature) channels. All of the computer code contained in Appendix A also uses this notation. Note that the $IQ_{calibrated}$ term defines σ_{NF}. Here, σ_{NF} is the "near field RCS," not the true RCS. True RCS is defined only as range to the target approaches infinity. When working with near field measurements, however, near field RCS can be a useful quantity to help understand the physical phenomena, and is used throughout this work. This near field RCS will have some error associated with it relative to the true RCS. NFFFTs seek to correct for this error.

3.2.2.5 Dual Calibration

A process called dual calibration was used to validate the measurements taken in the AFIT microwave laboratory and compare them to known scattering solutions. In this process, two different calibration standards are required, preferably of different geometries, such as a sphere and a cylinder. For the first calibration device, a 6-inch diameter sphere was used. The exact solution for the sphere was obtained using a Matlab function written for this purpose in 2005 by Capt. Jonathan E. Luminati. This code is

included in Appendix A. The second calibration standard was a squat cylinder with a 4.5-inch diameter. The exact solution for this specific cylinder was obtained from Capt. Gary Krupp, who generated the simulated RCS using a body-of-revolution solver code. For dual calibration, target and background measurements are taken of both calibration devices. One set of measurements is used as the target measurements and one set is used as the calibration target measurements. Whichever device was used as the calibration target, that device's exact solution is used as the exact solution for the dual calibration, according to Equation 20. This resulting RCS can then be compared to the exact RCS to gauge the error levels inherent in the measurement system.

Measurements of both the sphere and the squat cylinder were taken, and the dual calibration was performed. For these measurements, the HP 8510's maximum averaging of 4096 samples and maximum dwell time of 250 ms were used. Figure 10 shows the Method of Moments (MoM)/exact and measured RCS of the squat cylinder calibrated using the sphere. Figure 11 shows the exact and measured RCS of the sphere, calibrated using the squat cylinder. Note that the RCS scales on these figures are fairly small. The measured RCS tracks the exact solution fairly well in both cases. Given the level of averaging in the measurements, it is unlikely that the error between the measured and exact RCS is due to noise. It is far more likely that the error is due mostly to clutter that is not removed by the time gate. For instance, returns from the chamber floor, ceiling, and pedestal fall inside the time gate. These clutter returns cannot be perfectly subtracted out using background subtraction because of interactions and multiple scattering effects. It is the researcher's opinion that a major chamber redesign would be required to achieve

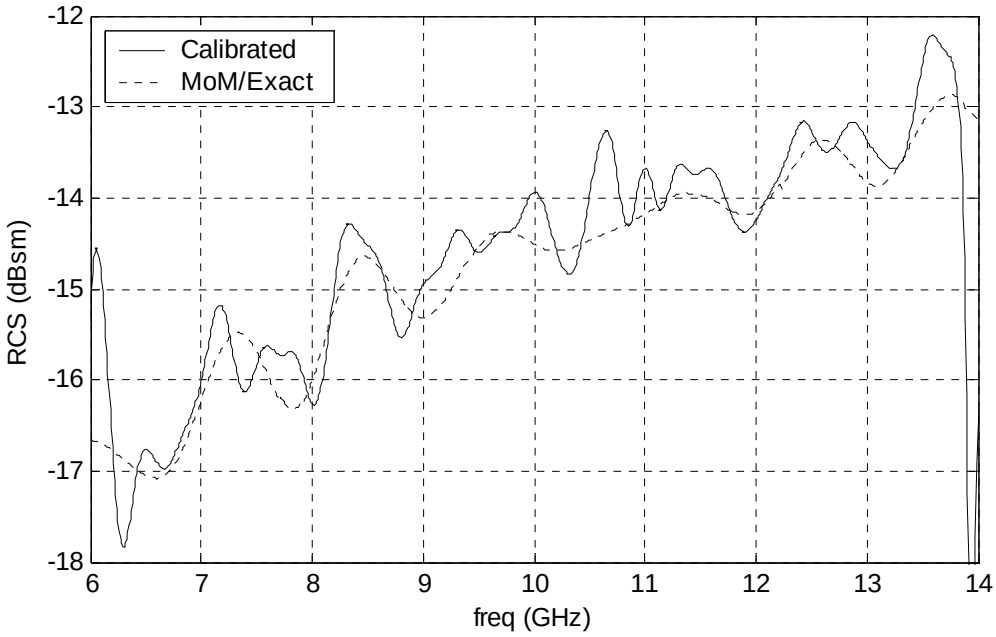

Figure 10. Measured and MoM/exact RCS for the 4.5-inch squat cylinder, calibrated using the 6-inch sphere.

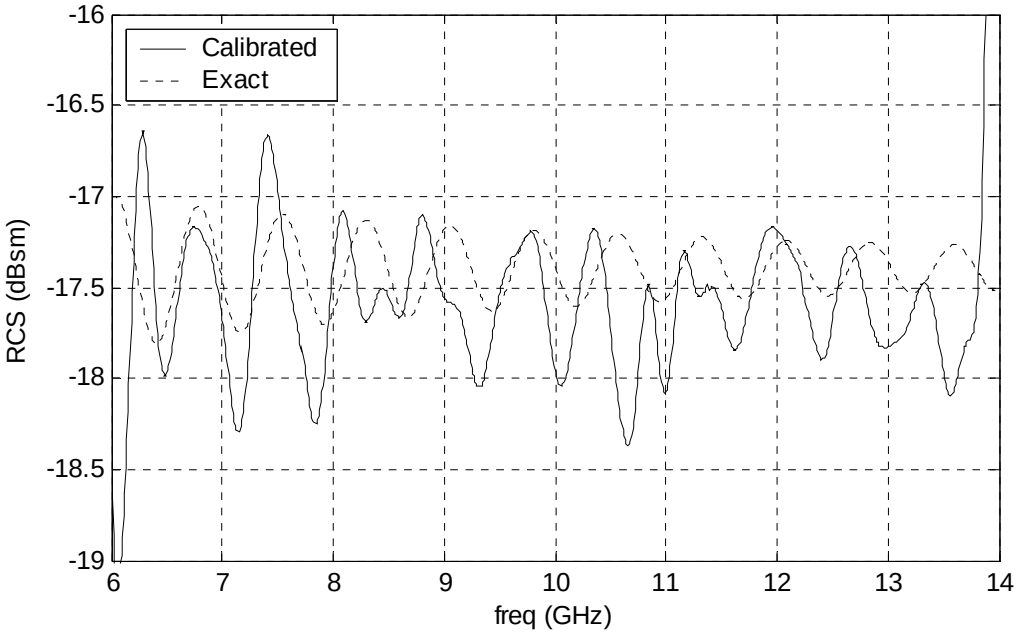

Figure 11. Measured and exact RCS for the 6-inch sphere, calibrated using the 4.5-inch squat cylinder.

results significantly better than those presented in Figure 12. These errors are being accepted as within acceptable limits.

3.2.2.6 Background Characterization

Another important aspect of chamber characterization is background characterization. This is performed to determine how stable the background is over time. In order to accomplish this, multiple measurements of the same background (empty chamber) are taken at different time instances, and these are subtracted from another instance of the background. A sample measurement of a calibration sphere minus the same background is also included. This background characterization routine indicates not only background stability, but also the level to which targets may be discriminated through background subtraction. Figure 13 displays the result of the background characterization. For clarity, two traces are shown. Note that the two instances of background measurement subtract to about the -85 dB level. The target return subtracts to 15 to 20 dB higher than this. From these results, the chamber is assumed to have a fairly stable background over this bandwidth, with good target separation. For these measurements, the HP 8510's maximum averaging of 4096 samples and maximum dwell time of 250 ms were used. Worse results would be expected for lower values of averaging.

3.3 Improved CNFFFT Implementation

When this research began, the NFFFT presented in "Overview of an Image-Based Technique for Predicting Far Field Radar Cross-Section from Near Field Measurements"

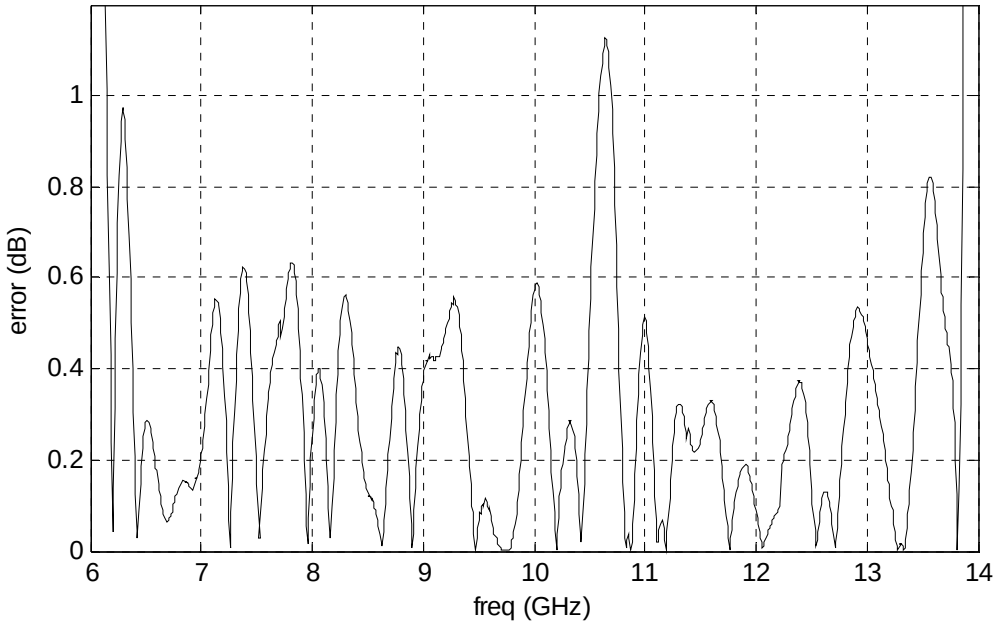

Figure 12. Absolute difference between measured and exact RCS for the dual calibration.

(LaHaie, 2003) was planned for use in this research. However, in 2005, Dr. LaHaie and his colleagues published a newer version of the IB NFFFT in "An Improved Version of the Circular Near Field to Far Field Transformation (CNFFFT)" (LaHaie, 2005). Since this newer version of the transformation "avoids the stationary phase approximation inherent in earlier versions," (LaHaie, 2005) I decided to use the newer version. For a complete derivation of this transformation, see LaHaie's article.

The first step of the transformation is to take a scaled derivative of the near field data with respect to wavenumber according to (LaHaie, 2005)

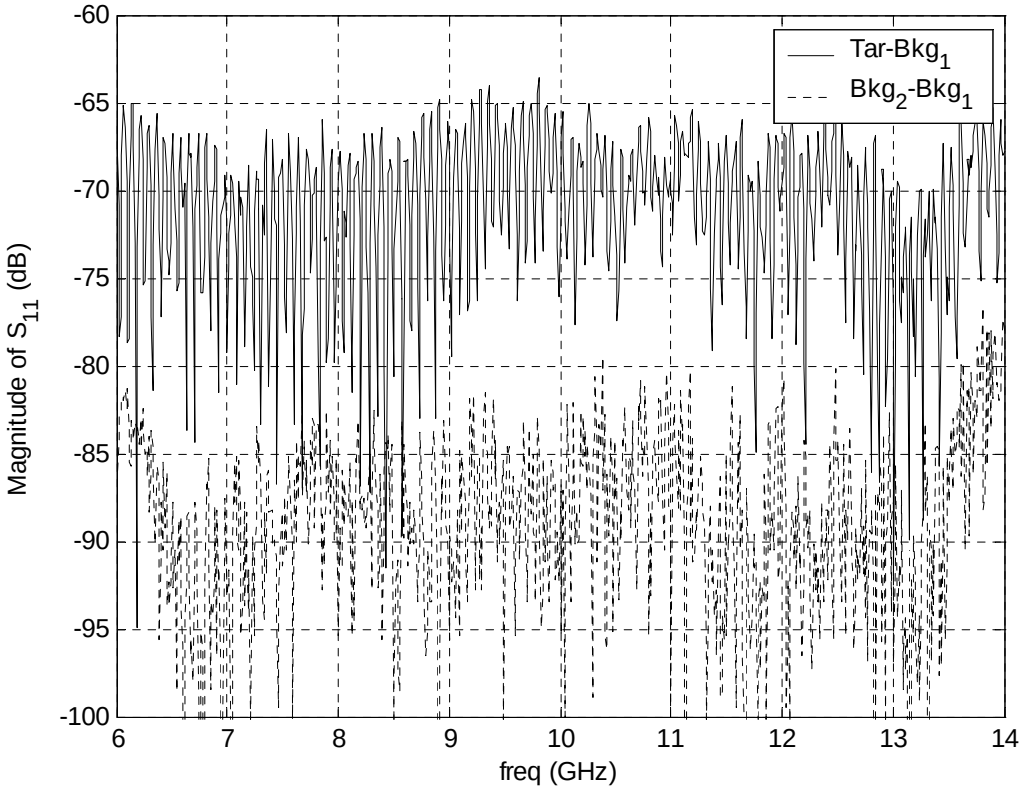

Figure 13. Background characterization. First time instance of background is subtracted from another instance of background and a measurement of the 6-inch sphere.

$$
\begin{aligned}
U'(\phi,k) &= \sqrt{\frac{i\pi k}{\rho_0}} \int R_0^2 H_0^{(2)}(2kR_0) \int u(\phi,k') e^{i2k'R_0} dk' dR_0 \\
&= \frac{1}{(4\pi)^2} \sqrt{\frac{i\pi k}{\rho_0}} \iint \gamma(\rho',\phi') H_0^{(2)}(2kR)\, \rho' d\rho' d\phi',
\end{aligned}
\tag{21}
$$

where (ρ_0,ϕ) is the measurement antenna position, ρ_0 = constant is the measurement radius, and ϕ is the azimuth angle on the measurement circle. Here, the measured monostatic backscattered field is given by

$$u(\phi,k)=\iint \gamma(\rho',\phi')\frac{e^{-i2kR}}{(4\pi R)^2}\rho' d\rho' d\phi', \qquad (22)$$

where γ is the target reflectivity distribution, and (ρ',ϕ') is a point on the target, and

$$R=\sqrt{\rho_0^2+\rho'^2-2\rho_0\rho'\cos(\phi-\phi')}. \qquad (23)$$

LaHaie (LaHaie, 2005) defines the monostatic far field scattering pattern in the waterline plane to be

$$S_{FF}(\phi,k)=\frac{1}{4\pi}\iint \gamma(\rho',\phi')e^{i2k\rho'\cos(\phi-\phi')}\rho' d\rho' d\phi', \qquad (24)$$

and the far field waterline RCS is related to the far field scattering pattern by

$$\sigma(\phi,k)=4\pi\left|S_{FF}(\phi,k)\right|^2. \qquad (25)$$

Using the large argument approximation for the Hankel function, Equation 21 can be simplified to

$$U'(\phi,k)=\frac{1}{\pi\sqrt{\rho_0}}\int R_0^{3/2}e^{-i2kR_0}\int u(\phi,k')e^{i2k'R_0}dk'dR_0, \qquad (26)$$

which can be implemented using a pair of 1-D discrete Fourier transforms. The rest of the transform can then be accomplished by (LaHaie, 2005)

$$S_{FF}(\phi,k) = 2\sqrt{\frac{\rho_0}{i\pi k}} \sum_{n=-N}^{N} \frac{(-i)^n e^{-in\phi}}{H_n^{(2)}(2k\rho_0)} \int_0^{2\pi} U'(\phi',k) e^{in\phi} d\phi'. \quad (27)$$

N is defined as $kD + 10$, where D is the maximum horizontal dimension of the target. According to LaHaie, Equation 27 "can be easily implemented with a pair of 1-D FFTs in the azimuth angle dimension" (LaHaie, 2005). The innermost integral is implemented in Matlab as an inverse DFT along the angle dimension, but the author of this work fails to see at the present time how the sum from $-N$ to N can be implemented as a DFT, so the sum is currently implemented directly using a for loop. Once again, the large argument approximation for the Hankel function can be used to simplify Equation 27 further. See Appendix A for details of computer code implementation.

3.4 Far Field Simulation Technique

During the course of this research, the AFIT RCS range was experiencing an extended period of downtime to implement hardware changes. During this downtime, the range was unavailable for taking measurements. This downtime conflicted with the research schedule, making timely measurements of the 2-foot cylinder impossible. Since the far field scattering from simple objects is well known by the community, and far field data were only needed to compare to near field data transformed to the far field by the

improved CNFFFT algorithm, it was decided to use X-Patch to generate the far field data to use as truth.

The reader should be aware that X-Patch employs several approximations, such as PO, to arrive at a solution for RCS. Therefore, RCS data produced by X-Patch cannot be considered to be an exact solution. However, all of the scattering bodies that are examined in this work have fairly simple geometries, and it is a fair assumption that the RCS solution generated by X-Patch for the frequencies of interest will be reasonably good (to within a couple of dB). The locations and levels of the specular returns and sidelobes, as well as the locations of the nulls, are all that is absolutely necessary to complete the analysis of this research. In these chief angular regions of interest, X-Patch should produce results that are very accurate (less than a dB). In any event, this work will assume that the X-Patch predictions are correct. Testing this assumption will remain outside the scope of this research.

IV. Results and Analysis

4.1 Near Field Data

Due to time constraints and software difficulties, the averaging at each frequency point was reduced to 1024 samples from 4096. This reduction resulted in more reasonable measurement times. However, due to this decrease in averaging, another dual calibration and background subtraction (vertical polarization data) was performed to ensure that the measurement quality would still be good enough. Figures 14 and 15 show the dual calibration results. Figure 14 shows the measured and MoM/exact RCS for the 4.5-inch squat cylinder, and Figure 15 shows the measured and exact RCS for the 6-inch sphere. Figure 16 shows the error as a function of frequency between the measured and exact quantities. As these figures illustrate, these dual calibration results are actually better than those presented in chapter three that were taken with maximum averaging. This is a strong indication that the largest source of error is not noise, but rather chamber clutter.

In the background characterization, which is shown in Figure 17, the results of decreased averaging become more apparent. Whereas the different time instances of the background were subtracting to around the -85 to -90 dB level with higher averaging, 1024 sample averaging yields levels as high as -72 dB at certain frequencies. Between 10 and 13 GHz, however, the two instances of background still subtract to about the -85 dB level. This odd frequency behavior can not be fully explained.

The 2 ft. long cylinder was placed in the chamber horizontally, so that 0° points the cylinder's broadside toward the horn antenna. It follows that at 90° and 270°, the flat circular end cap points toward the horn. Note that when the cylinder is oriented

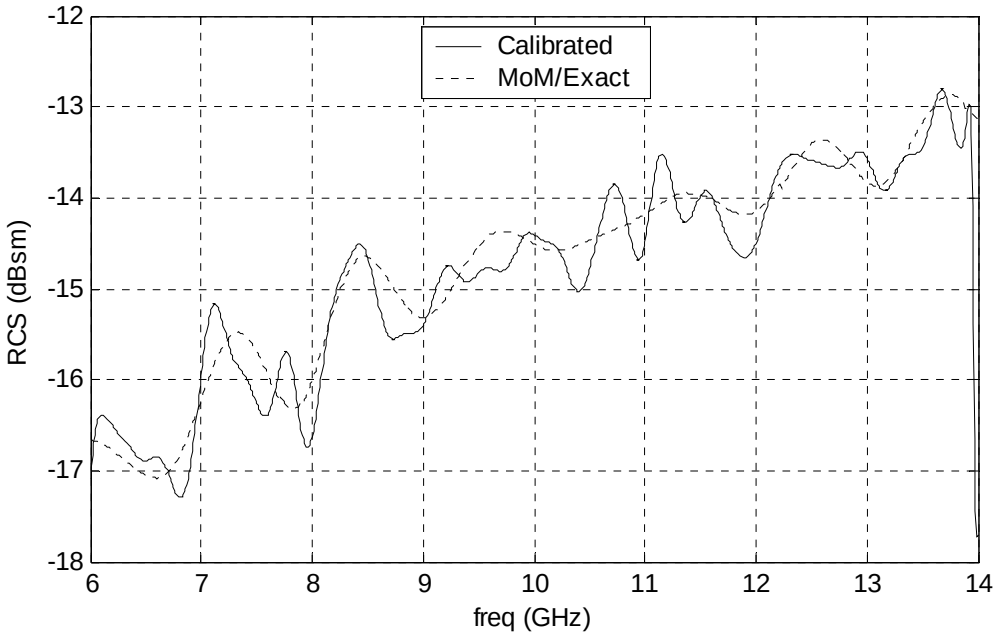

Figure 14. Calibrated and exact RCS for a 4.5-inch squat cylinder, v-pol. Cylinder RCS was calibrated using a 6-inch sphere.

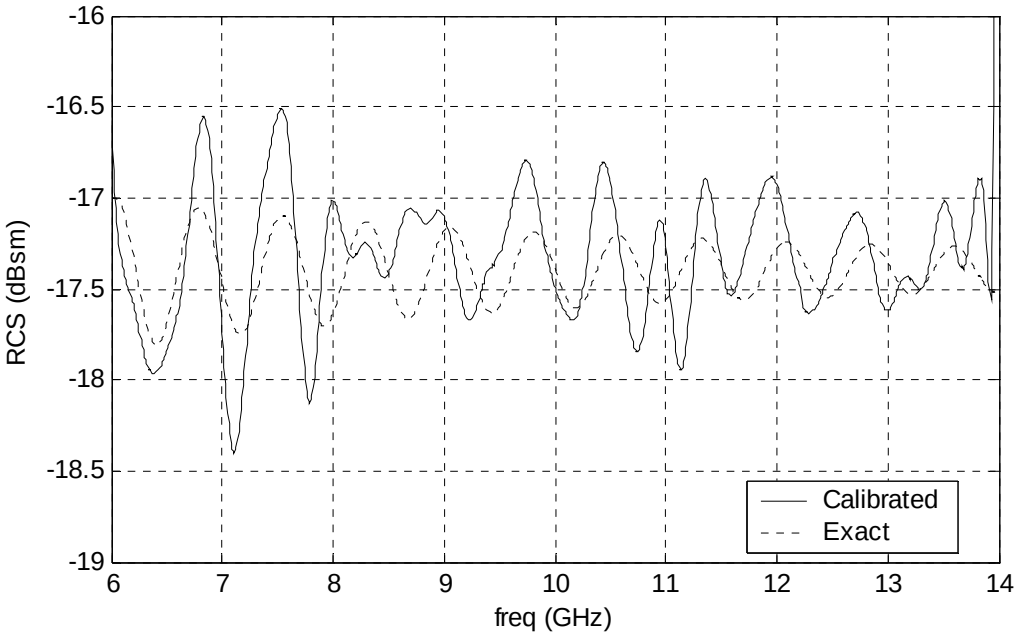

Figure 15. Calibrated and exact RCS for a 6-inch sphere, v-pol. Sphere RCS was calibrated using a 4.5-inch squat cylinder.

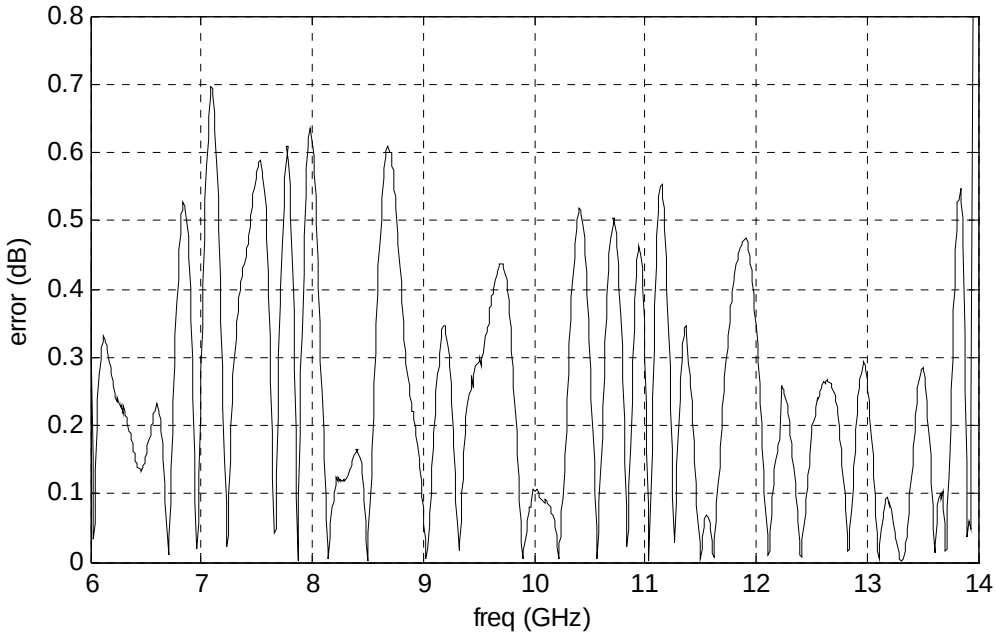

Figure 16. Absolute difference between calibrated and exact RCS for v-pol dual calibration using a 6-inch sphere and a 4.5-inch squat cylinder.

such that the end caps face the horn antenna, the cylinder actually meets the far field criterion defined by Equation 1, since the cylinder has a diameter of three inches. In these configurations, the near field RCS and the far field RCS predictions from X-Patch should agree very well. The cylinder and the background measurements were performed for both polarizations, and the near field data were calibrated using the techniques presented in chapter three. Both near field RCS and phase plots of the near field data were generated. The phase information can be very informative and helpful in interpreting the results of the CNFFFT, since the CNFFFT is a phase-based transformation. The near field RCS plot for vertical polarization, 10 GHz is shown in Figure 18. Figure 19 shows the near field phase data for the vertical polarization, 10 GHz. Figures 20 and 21 show the same plots, only for horizontal polarization. Near field

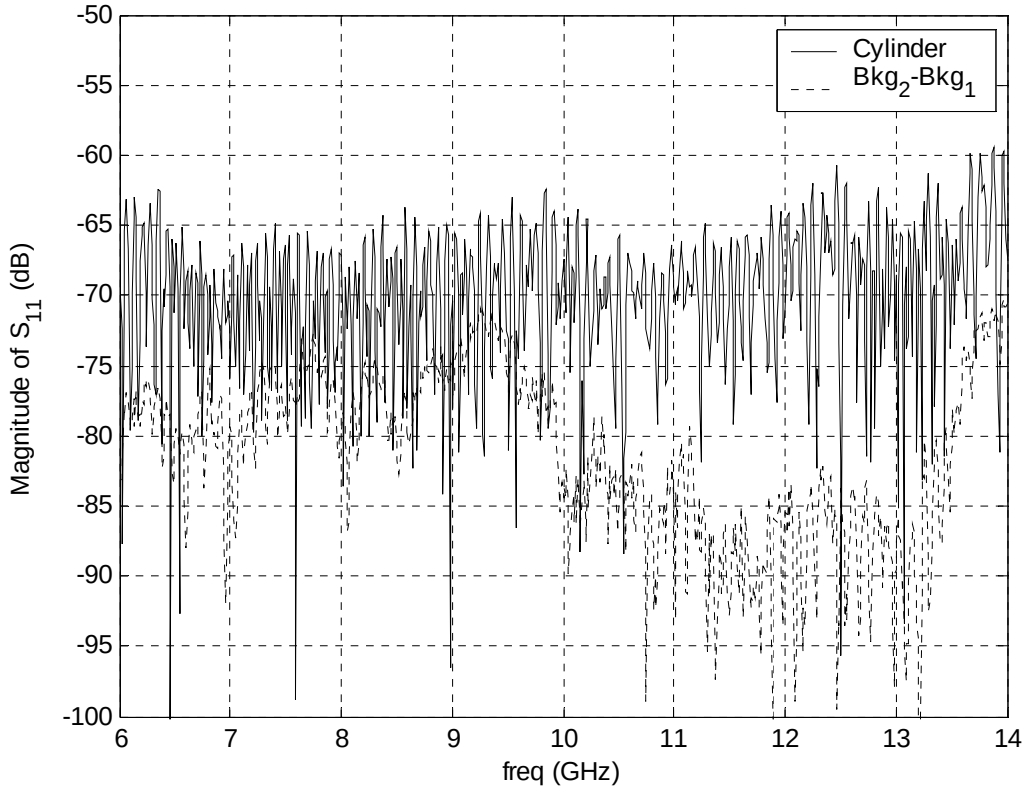

Figure 17. Magnitude of reflection for a 4.5-inch squat cylinder after background subtraction and the difference of two time instances of background.

RCS and phase plots for both polarizations at 6.5 GHz and 13.5 GHz are contained in Appendix B (Figures 25 through 32). Note that the 500 MHz on either end of the bandwidth is discarded before the data are put through the CNFFFT algorithm. The reason for this decision is due to the lack of infinite sampling in frequency. The data are post-processed in Matlab (software gated), and the DFT pair causes the data to lose accuracy near the band endpoints. Good behavior was observed everywhere except in the 500 MHz at either end of the 6 to 14 GHz band, so the frequencies near the endpoints were discarded.

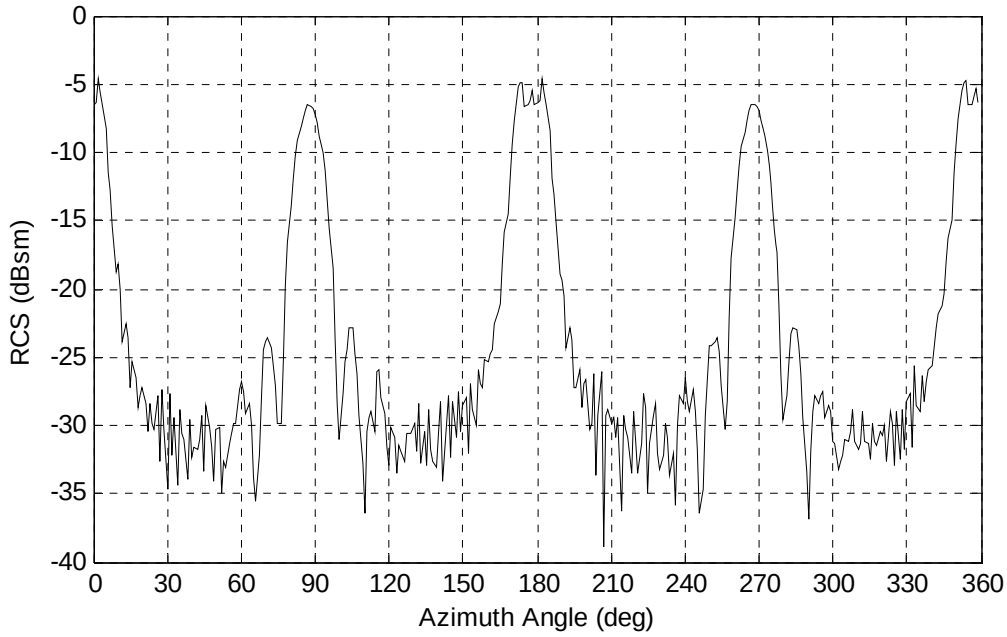

Figure 18. Near field RCS of 2-foot cylinder, v-pol, 10 GHz.

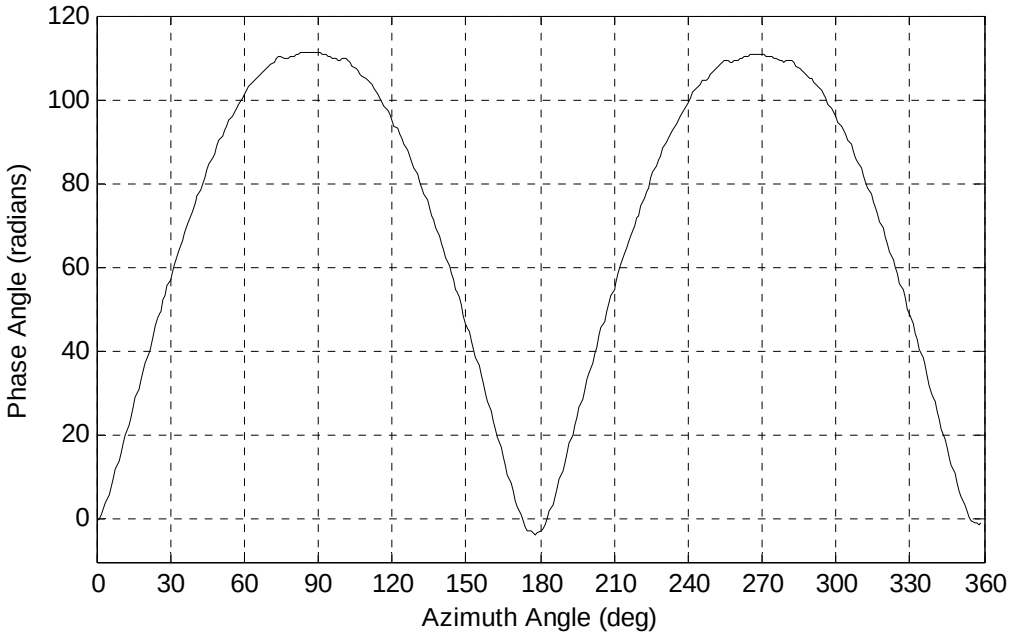

Figure 19. Near field phase data of 2-foot cylinder, v-pol, 10 GHz.

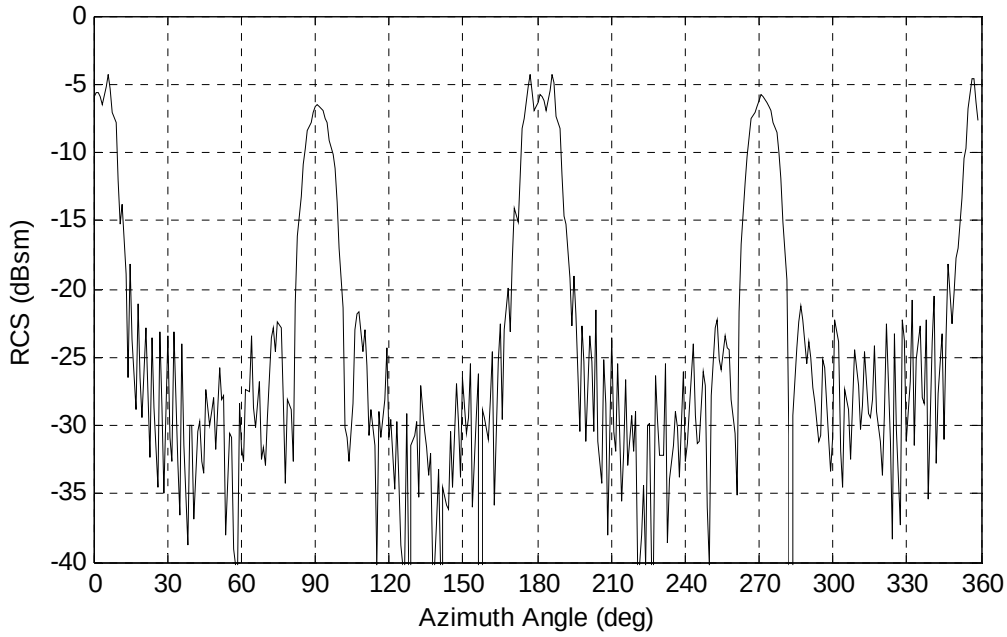

Figure 20. Near field RCS of 2-foot cylinder, h-pol, 10 GHz.

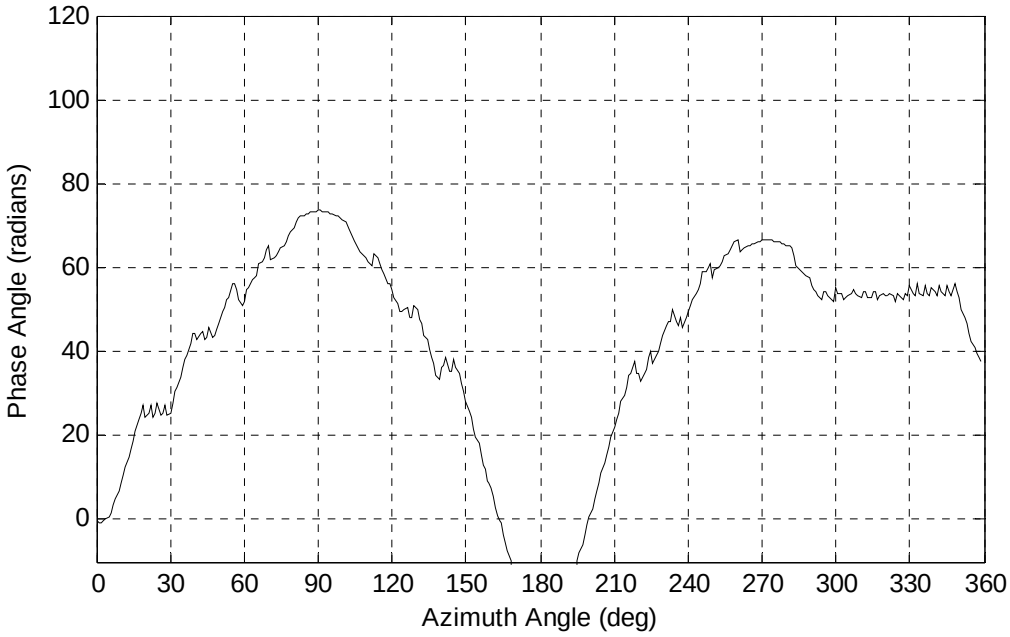

Figure 21. Near field phase data of 2-foot cylinder, h-pol, 10 GHz.

The near field RCS plots show results as expected. Using hip-pocket predictions from *Radar Cross Section* (Knott, 2004), the cylinder at broadside should have an RCS of 4.7 dBsm. When the cylinder is oriented end on, such that only the circular flat end cap is visible, the RCS should be -5.4 dBsm. For the end on case, the near field RCS is very close to this hip-pocket prediction, as expected. Also as expected, the near field RCS is about 10 dB below the hip-pocket calculation for the broadside case. This is expected due to the spherical nature of the waves incident on the cylinder in the near field case. A specular return is observed over a much wider angular extent when the cylinder is close to the probe antenna. In the far field case, the scattered field at broadside is concentrated into a much narrower sector, based on frequency. The lower the frequency, the wider this main beam will be. This frequency dependent behavior is seen in the 6.5 GHz and 13.5 GHz plots located in Appendix B.

The phase plots (Figures 19 and 21) exhibit different behavior from one another. The vertical polarization phase information appears much smoother whereas the horizontal polarization phase data contains some discontinuous behavior. Notice that this behavior seems to be worse at higher frequencies and less pronounces at the lower frequencies. See Appendix B for the 6.5 GHz and 13.5 GHz near field phase plots. Even the vertical polarization data exhibits this discontinuous behavior in the 13.5 GHz plot. This phase discontinuity is likely responsible for the fact that the noise floor in the RCS plots is higher for the horizontal polarization than for vertical polarization.

4.2 Far Field Data

A facet model of the 2-ft. cylinder with assistance from Capt. Gary Krupp, and this facet file was used as an input to X-Patch. The material was specified as perfectly conducting, which is a reasonably good approximation for aluminum from 6 to 14 GHz. Far field data were generated for each point in azimuth where the near field measurements were taken; the same number of points and sample spacing was used. Simulations were run for the center frequency, 10 GHz, as well as the two frequency endpoints, 6.5 GHz and 13.5 GHz. Figure 22 shows the X-Patch far field RCS prediction for the cylinder at 10 GHz. For all simulations, no extra diffraction calculations were performed, and the scattering was calculated using the PO method. Due to this fact, the X-Patch RCS prediction is the same for both polarizations. The X-Patch predictions match up well with the hip-pocket predictions mentioned in the previous section, as expected.

4.3 NFFFT-FF Comparison

At present, the improved CNFFFT algorithm is not correctly implemented. The Matlab code does output an RCS prediction, but this prediction deviates significantly in pattern from the X-Patch prediction. The RCS values in certain sectors seem to be approximately the correct level, however. Figures 23 and 24 display the RCS predicted by the CNFFFT for the vertical polarization and horizontal polarization near field data, respectively.

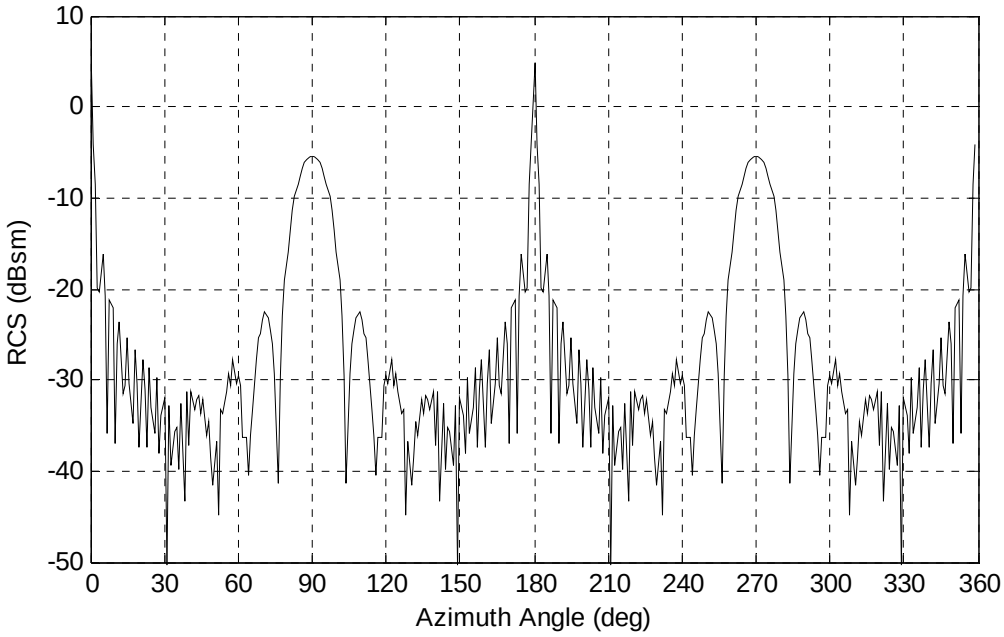

Figure 22. X-Patch far field RCS of 2-foot cylinder, 10 GHz.

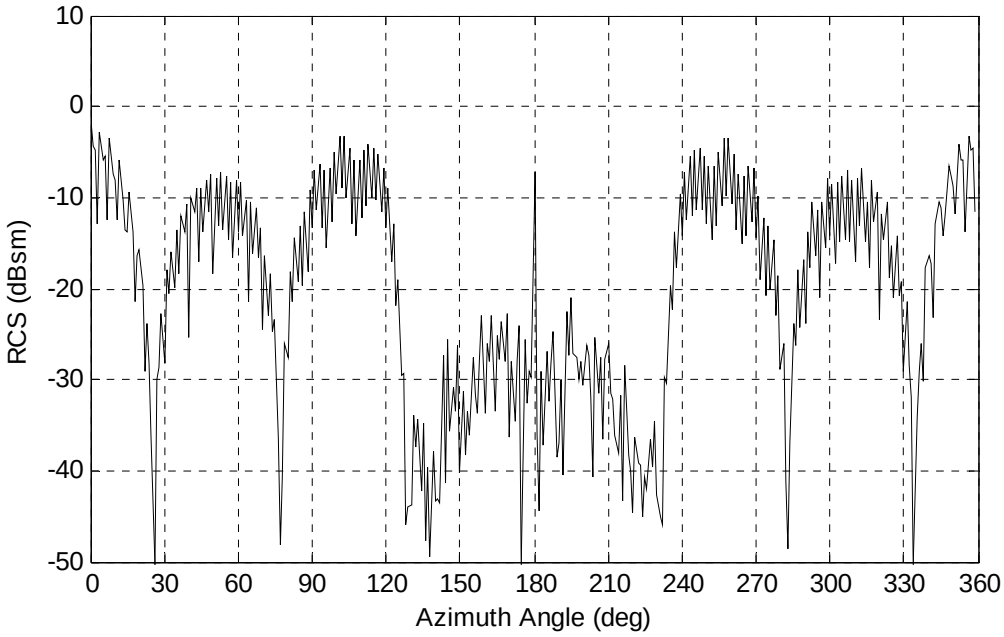

Figure 23. Near field data transformed to far field RCS, v-pol, 10 GHz.

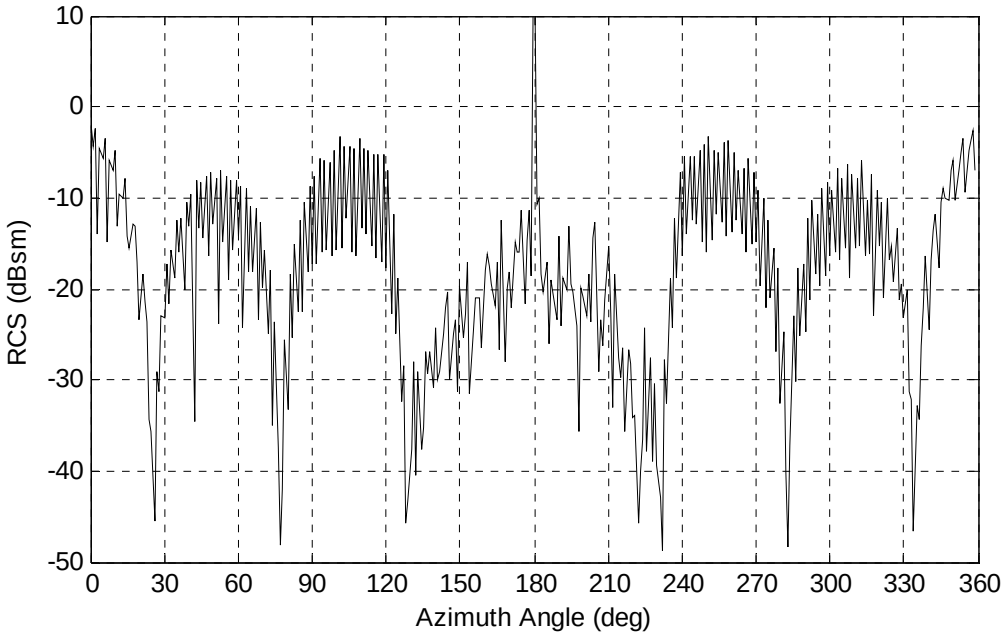

Figure 24. Near field data transformed to far field RCS, h-pol, 10 GHz.

V. Conclusions and Recommendations for Future Work

To summarize, the AFIT microwave laboratory's anechoic chamber was adapted to perform near field scattering measurements. The chamber was characterized to determine the level of error that is expected in the near field RCS. In short, a system was developed to obtain calibrated near field scattering measurements. Actual measurements were obtained of both polarizations for a two foot long metal cylinder. Far field data were generated by simulation in X-Patch. The improved CNFFFT was implemented in Matlab, but at this time, the code does not appear to be implemented correctly. Further analysis involving the transformation itself or near field data transformed to the far field by the algorithm cannot continue until the Matlab script that performs the improved CNFFFT is shown to be working properly. It is still possible that the code is functioning

correctly, but that there is too much phase error in the measured near field data to transform well.

Putting the code through an extensive troubleshooting process could confirm whether the large FF errors arise from phase errors in the NF data or from errors in the CNFFFT implementation. To begin this process, a simple simulation should be performed to create artificial NF data. A linear string of point scatterers would serve this purpose. Placing the transmitter/receiver close to the string of point scatterers would yield NF data, while placing it much farther away would yield the FF return. Using the simulated NF data as an input to the CNFFFT code, it could be quickly verified whether or not the algorithm is implemented correctly. If incorrect FF results are still observed using the simulated data, then the error is due to the code and not due to corrupt phase information in the measured data.

Future work in this area should involve measurements of additional scatterers. For this thesis, only a cylindrical target was examined. There are many other geometries that could be examined, such as vertically and horizontally aligned flat plates. The largest limiting factor in determining what objects can be tested using the system laid out in this work is the size of the potential objects. To be compatible with this research, the scattering body must meet the far field criterion in the vertical direction, which means it cannot be more than a few inches tall. It must also fail to meet the far field criterion in the horizontal direction, but cannot exceed about two feet in length due to the space constraints and clutter environment of the chamber.

When dealing with actual measurements, there is always the difficulty of trying to separate the errors inherent in the measurements from the errors due to the transformation

algorithm. If a better study of the algorithm's errors is desired, it may be a better course of action to conduct such a study using simulated near field data. Of course, simulated data will also have errors present, but these errors may be easier to quantify and account for. Future work in this area could also focus on taking the near field collection methodology laid out in this work and improving on it. Such a task might require upgrades to the available facilities, or a complete redesign of the equipment and software.

Appendix A: Computer Code

```
% readtar_RASCAL.m
function output=readtar_RASCAL(filename)
%-------------------------------------------------------
% This function reads the ASCII data output of the
% RASCAL NF chamber and outputs the I & Q channels into
% a complex scattering matrix.  The locations of the
% spatial sampling points and the frequency list is
% also included in the output
% -------------------------------------------------------

fid=fopen(filename,'r');

% Get Number of Points in Frequency & Space from Header
x=fgetl(fid); %discard 1st line of header
x=fgetl(fid); %2nd line contains # of spatial points
i=0;
while ~isspace(x(end-i))
    temp(i+1)=x(end-i);
    i=i+1;
end %defines str containing # points in space
numspacepts_str=char(fliplr(temp));
numspacepts=str2num(numspacepts_str);
x=fgetl(fid); %discard 3rd line of header
x=fgetl(fid); %discard 4th line of header
x=fgetl(fid); %5th line contains # of frequency points
i=0;
while ~isspace(x(end-i))
    temp(i+1)=x(end-i);
    i=i+1;
end %defines str containing # points in freq
numfreqpts_str=char(fliplr(temp));
numfreqpts=str2num(numfreqpts_str);
clear i temp numspacepts_str numfreqpts_str;
for i=1:8,x=fgetl(fid);end % Discard Rest of Header

% Read Data
for sp=1:numspacepts
    x=fgetl(fid); % Discard Blank
    x=fgetl(fid); % Read space point info
    i=1;
    while ~isspace(x(i)) % Read space point location
        temp(i)=x(i);
        i=i+1;
    end
    spacepts(sp)=str2num(temp); % Save Space List
    clear temp;
    x=fgetl(fid); % Discard Blank
    for fp=1:numfreqpts
        x=fgetl(fid); % Read line
        tempfreqdata(fp,:)=str2num(x);
    end
    if sp==1,freqpts=tempfreqdata(:,1);end % Save Frequency List
    iqmatrix(:,sp)=complex(tempfreqdata(:,2),tempfreqdata(:,3));
```

```
    clear tempfreqdata;
end

fclose(fid);

% Save Outputs
output.spacepts=spacepts;
output.freqpts=freqpts;
output.iq=iqmatrix;

return
% END OF CODE ----------------------------------------


% genfig_RASCAL.m
%-------------------------------------------------------------
% This script generate figures from data output from the RASCAL
% NF chamber.  The ASCII files are read in using the function
% readtar.m (See readtar.m for details)
%-------------------------------------------------------------

clear;clc;close all hidden;

temp=fopen('spheredata.mat','r'); %see if data file exists
spheredata_flag=temp; %create flag from results
if temp~=(-1),fclose(temp);,end; %close file if it exists

if spheredata_flag==(-1)
    sphere_tar=readtar('sphere_tar.txt'); %read target data
    sphere_bkg=readtar('sphere_bkg.txt'); %read background data
    save spheredata %saves data in binary form for speed later
else
    load spheredata %uses saved data instead, if file exists
end

iq=sphere_tar.iq-sphere_bkg.iq; %background subtraction
iq_td=ifft(iq,[],1);

x=linspace(-25,25,101); %position vector
f=linspace(8e9,12e9,401).'; %frequency vector
deltaf=f(2)-f(1); %frequency step size
B=f(end)-f(1); %measurement bandwidth
t=linspace(1/B,1/deltaf,401).'; %time vector for TD plots

figure(1);
pcolor(x,t/1e-9,20*log10(abs(iq_td))),shading flat
xlabel('x-Position (in)')
ylabel('Time (ns)')
colorbar
set(gcf,'paperposition',[0.25 4 6 4.5])

bkgiq_td=ifft(sphere_bkg.iq,[],1);

figure(2);
pcolor(x,t/1e-9,20*log10(abs(bkgiq_td))),shading flat
```

```
xlabel('x-Position (in)')
ylabel('Time (ns)')
colorbar
set(gcf,'paperposition',[0.25 4 6 4.5])

figure(3);
subplot(2,1,1)
plot(f/1e9,20*log10(abs(iq(:,51))),'k'),hold on,grid on
plot(f/1e9,20*log10(abs(sphere_bkg.iq(:,51))),'k:')
xlabel('Frequency (GHz)'),ylabel('Magnitude of S_1_1')
legend('tar-bkg','bkg',4)
subplot(2,1,2)
plot(t/1e-9,20*log10(abs(iq_td(:,51))),'k'),hold on,grid on
plot(t/1e-9,20*log10(abs(bkgiq_td(:,51))),'k:')
xlabel('Time (ns)'),ylabel('Magnitude of S_1_1')
legend('tar-bkg','bkg',4)
set(gcf,'paperposition',[0.25 4 6 4.5])
% END OF CODE -----------------------------------------


% testgate.m
%-----------------------------------------------------------------------
% This function tests the new time gate and window functions by
applying
% them to the exact solutions for a 6" sphere and a 4.5" cylinder.
% If they perform well, the windowed and gated solution should track
% the exact solution very closely.  The gate and window functions are
% also displayed.
%-----------------------------------------------------------------------

clear;clc;close all hidden;

load sph6in_6_14_exact
load cyl450_6_14_vv_exact

f=linspace(6e9,14e9,801).';
t=linspace(0,1/(f(2)-f(1)),801).';

win=hamming(801);
tg=blackman(41); %roll-off portion of time gate
gate=[zeros(370,1);tg(1:21);ones(19,1);tg(21:41);zeros(370,1)]; %gate
function

%sph_ex_g=fft(ifftshift(gate.*fftshift(ifft(win.*sph6in_6_14_exact))));
%cyl_ex_g=fft(ifftshift(gate.*fftshift(ifft(win.*cyl450_6_14_vv_exact))
));
sph_ex_g=fft(ifftshift(gate.*fftshift(ifft(sph6in_6_14_exact))));
cyl_ex_g=fft(ifftshift(gate.*fftshift(ifft(cyl450_6_14_vv_exact))));


figure
plot(f/1e9,20*log10(abs(sph6in_6_14_exact)),'k:'),grid on,hold on
axis([6 14 -17.9 -16.9])
xlabel('freq (GHz)'),ylabel('RCS (dBsm)')
%title('Sphere RCS, Exact vs. Time Gated Exact (New Gate)')
```

```
plot(f/1e9,20*log10(abs(sph_ex_g)),'k')
%plot(f/1e9,20*log10(abs(sph_ex_g./win)),'k')
legend('Exact','Gated Exact')
set(gcf,'paperposition',[0.25 4 6 4.5])

figure
plot(f/1e9,20*log10(abs(cyl450_6_14_vv_exact)),'k:'),grid on,hold on
axis([6 14 -17.5 -12.5])
xlabel('freq (GHz)'),ylabel('RCS (dBsm)')
%title('Cylinder RCS, Exact vs. Time Gated Exact (New Gate)')
plot(f/1e9,20*log10(abs(cyl_ex_g)),'k')
%plot(f/1e9,20*log10(abs(cyl_ex_g./win)),'k')
legend('Exact','Gated Exact',0)
set(gcf,'paperposition',[0.25 4 6 4.5])

figure
subplot(2,1,1),plot(f/1e9,win,'k'),grid on
xlabel('freq (GHz)'),ylabel('Magnitude')
%title('Hamming Window')
axis([6 14 0 1.2])

subplot(2,1,2),plot(t/1e-9,gate,'k'),grid on
xlabel('t (ns)'),ylabel('Magnitude')
%title('Time Gate')
axis([0 100 0 1.2])
set(gcf,'paperposition',[0.25 4 6 4.5])
% END OF CODE ------------------------------------------------------


% bistatic.m (Written by Capt. Jonathan E. Luminati, 2005)
%-------------------------------------------------------------------------
% function [iq] = bistatic_exact(dia,pol,freq,theta);
%
% Calculates the scaled ratio of scattered-to-incident E-fields
% (Es/Ei) for a sphere.  It assumes the TX horn, sphere, and
% RX horn define the "scattering plane."  The unit vector
% corresponding to the direction of TX propagation is defined
% along the +z direction.   The unit vector corresponding to
% the linearly polarized E-field of the TX wave is defined
% along the +x direction.
%
% Input:
%   dia     : sphere diameter, inches
%   pol     : polariazation, 1=HH, 2 = VV, 3 = HV, 4 = VH
%   freq    : frequencies required, Hz
%   theta   : angle between the TX propagation vector and the RX
%             propagation vector, deg.
%               theta = 0 implies forward scattering
%               theta = 180 implies backscatting (monostatic)
%
% Output:
%   iq      : 2*sqrt(pi)*r*Es/Ei
%
% Coordinate systems and scattered field equations are taken from
% Harrington, "Time-Harmonic Electromagnetic Fields"
```

```
%
% Written by Jonathan E. Luminati, 2005

function [iq] = bistatic(dia,pol,freq,theta);

% define speed of light, m/s
C = 3e8;

% ensure theta between 0 and 180 and then convert to radians
theta = mod(theta,360);
if theta>180
    theta = 360-theta;
end
theta = theta*pi/180;

% ensure freq vector oriented horizontally
if size(freq,2)==1
    freq = freq';
end

% convert sphere diameter to meters
a = dia/2*0.0254;

% set number of terms in sum
n_max = 100;
n = [1:n_max]';
n_ext = [0:n_max]';

% calculate a_n
a_n = repmat(j.^-n.*(2*n+1)./n./(n+1),1,length(freq));

% calculate k_a
k_a = 2*pi*freq/C*a;

% get required sherical Bessel/Hankle functions
J_sphere = zeros(n_max+1,length(freq));
H_sphere = zeros(n_max+1,length(freq));
for i = 1:n_max+1
    J_sphere(i,:) = besselj(i+0.5,k_a);
    H_sphere(i,:) = besselh(i+0.5,2,k_a);
end
J_sphere = sqrt(pi*repmat(k_a,n_max+1,1)/2).*J_sphere;
H_sphere = sqrt(pi*repmat(k_a,n_max+1,1)/2).*H_sphere;
J_sphere_prime = -J_sphere(2:end,:) +
repmat(n+0.5,1,length(freq))./repmat(k_a,n_max,1).*J_sphere(1:end-1,:);
H_sphere_prime = -H_sphere(2:end,:) +
repmat(n+0.5,1,length(freq))./repmat(k_a,n_max,1).*H_sphere(1:end-1,:);

% calculate b_n
b_n = -a_n.*J_sphere_prime./H_sphere_prime;

% calculate c_n
c_n = -a_n.*J_sphere(1:end-1,:)./H_sphere(1:end-1,:);

% get required associated Legendre fucntions and derivatives
```

```
if theta==pi
    P_term = repmat((-1).^n.*n.*(n+1)/2,1,length(freq));
    P_prime_term = P_term;
else
    if theta==0
        theta=0.0001;
    end
    P = zeros(n_max+1,1);
    for i = 1:n_max+1
        temp = legendre(i,cos(theta));
        P(i)=temp(2);
    end
    P_prime_term = repmat(1/(cos(theta)^2-1)*(n.*P(2:end)-
(n+1)*cos(theta).*P(1:end-1)),1,length(freq))*sin(theta);
    P_term = repmat(P(1:end-1),1,length(freq))/sin(theta);
end

% calculate iq data
if pol == 1             % HH polarization
    iq =
j*C/sqrt(pi)./freq.*sum(repmat(j.^n,1,length(freq)).*(b_n.*P_prime_term
-c_n.*P_term),1);
elseif pol == 2         % VV polarization
    iq =
j*C/sqrt(pi)./freq.*sum(repmat(j.^n,1,length(freq)).*(b_n.*P_term-
c_n.*P_prime_term),1);
else                    % cross-polarization
    iq = 0;
end
% END OF CODE ------------------------------------------------------


% dualcal.m
%-------------------------------------------------------------
% This script reads in measured and exact data for the 6"
% sphere and the 4.5" squat cylinder and performs the dual
% calibration.  Also generated is a graph showing the error
% in decibels between the measured and exact RCS (same for
% both objects).
%-------------------------------------------------------------

clear;clc;close all hidden;

load rawdata_6_14
load cyl450_6_14_vv_exact
load sph6in_6_14_exact

t=linspace(0,1/(f(2)-f(1)),801).'; %time vector

win=hamming(801); %define window function
tg=blackman(41);
gate=[zeros(203,1);tg(1:21);ones(19,1);tg(21:41);zeros(537,1)]; %gate
function

cyl450_6_14_subiq=cyl450_6_14_tariq-cyl450_6_14_bkgiq; %subtract bkg
```

```
cyl450_6_14_subiq_td=ifft(win.*cyl450_6_14_subiq); %window & ifft
cyl450_6_14_subiq_g_td=gate.*cyl450_6_14_subiq_td; %apply time gate
cyl450_6_14_subiq_g=fft(cyl450_6_14_subiq_g_td); %fft to freq domain

sph6in_6_14_subiq=sph6in_6_14_tariq-sph6in_6_14_bkgiq; %subtract bkg
sph6in_6_14_subiq_td=ifft(win.*sph6in_6_14_subiq); %window & ifft
sph6in_6_14_subiq_g_td=gate.*sph6in_6_14_subiq_td; %apply time gate
sph6in_6_14_subiq_g=fft(sph6in_6_14_subiq_g_td); %fft to freq domain

cyl450_6_14_g_cal=sph6in_6_14_exact.*(cyl450_6_14_subiq_g)./...
    (sph6in_6_14_subiq_g); % calibrate the cylinder with the sphere
sph6in_6_14_g_cal=cyl450_6_14_vv_exact.*(sph6in_6_14_subiq_g)./...
    (cyl450_6_14_subiq_g); % calibrate the sphere with the cylinder

figure
plot(f/1e9,20*log10(abs(cyl450_6_14_g_cal)),'k'),grid on,hold on
plot(f/1e9,20*log10(abs(cyl450_6_14_vv_exact)),'k:')
xlabel('freq (GHz)'),ylabel('RCS (dBsm)')
%title('Cyl RCS (Cal w/ Sph) vs. MoM/Exact Cyl RCS (BW=8GHz), Max Avg &
Sweep Time')
legend('Calibrated','MoM/Exact',2)
axis([6 14 -18 -12])
set(gcf,'paperposition',[0.25 4 6 3.5])

figure
plot(f/1e9,20*log10(abs(sph6in_6_14_g_cal)),'k'),grid on,hold on
plot(f/1e9,20*log10(abs(sph6in_6_14_exact)),'k:')
xlabel('freq (GHz)'),ylabel('RCS (dBsm)')
%title('Sph RCS (Cal w/ Cyl) vs. Exact Sph RCS (BW=8GHz), Max Avg &
Sweep Time')
legend('Calibrated','Exact',2)
axis([6 14 -19 -16])
set(gcf,'paperposition',[0.25 4 6 3.5])

dualcalerror=abs(20*log10(abs(sph6in_6_14_g_cal))-...
    20*log10(abs(sph6in_6_14_exact)));

figure
plot(f/1e9,dualcalerror,'k'),grid on
xlabel('freq (GHz)'),ylabel('error (dB)')
%title('Error Between Measured (Dual-Cal) and Exact RCS')
axis([6 14 0 1.2])
set(gcf,'paperposition',[0.25 4 6 3.5])
% END OF CODE ------------------------------------------------



% bkgchar.m
%-----------------------------------------------------------------
% This script performs the background subtraction routine and
% generates the figure.
%-----------------------------------------------------------------

clear;clc;close all hidden;
```

```
% Read data in
load sph6in_6_14_tar.txt
load sph6in_6_14_bkg.txt
load sph6in_6_14_bkg2.txt
load sph6in_6_14_bkg3.txt
load sph6in_6_14_bkg4.txt
load sph6in_6_14_bkg5.txt

% Format data
tar=complex(sph6in_6_14_tar(3:end,3),sph6in_6_14_tar(3:end,4));
b1=complex(sph6in_6_14_bkg(3:end,3),sph6in_6_14_bkg(3:end,4));
b2=complex(sph6in_6_14_bkg2(3:end,3),sph6in_6_14_bkg2(3:end,4));
b3=complex(sph6in_6_14_bkg3(3:end,3),sph6in_6_14_bkg3(3:end,4));
b4=complex(sph6in_6_14_bkg4(3:end,3),sph6in_6_14_bkg4(3:end,4));
b5=complex(sph6in_6_14_bkg5(3:end,3),sph6in_6_14_bkg5(3:end,4));

f=linspace(6e9,14e9,801).'; %frequency vector

% Perform subtractions
b21=b2-b1+eps; %bkg2 - bkg1
b31=b3-b1+eps; %bkg3 - bkg1
b41=b4-b1+eps; %bkg4 - bkg1
b51=b5-b1+eps; %bkg5 - bkg1
tb=tar-b1+eps; %tar-bkg1

figure %For clarity of figure, only two traces are displayed
plot(f/1e9,20*log10(abs(tb)),'k',...
     f/1e9,20*log10(abs(b21)),'k:')
%     f/1e9,20*log10(abs(b31)),'b',...
%     f/1e9,20*log10(abs(b41)),'b',...
%     f/1e9,20*log10(abs(b51)),'b')
axis([8 12 -100 -60])
xlabel('f (GHz)')
ylabel('Magnitude of S_{11} (dB)')
%title('Tar-Bkg_1 & Bkg_2-Bkg_1')
legend('Tar-Bkg_1','Bkg_2-Bkg_1')
grid on
set(gcf,'paperposition',[0.25 4 6 4.5])
% END OF CODE ------------------------------------------------



% cnffft.m
%-----------------------------------------------------------
% Performs the Improved CNFFFT on a NF Scattering Data Set
% In this case, the NF scattering data of the 2ft bar
%-----------------------------------------------------------
clear;clc;close all hidden;

c=299792458; %speed of light (m/s)

load bar_calibrated

u=bar_g_cal(51:751,:); %discard endpoints, keep 6.5GHz-13.5GHz
clear bar_g_cal
```

```
f=linspace(6.5e9,13.5e9,701).'; %frequency vector (Hz)
t=linspace(0,1/(f(2)-f(1)),701).'; %time vector (s)
az=linspace(0,359,360); %azimuth vector (degrees)
azrad=az*pi/180; %azimuth vector (radians)
k=2*pi*f/c; %k vector (1/m)
R0=c*t/2; %range vector (m)

ifftu=ifft(u,[],1);

% 191.5cm horn to pedestal center, so shift NF data in time so that t=0
% occurs as close to 1.915m downrange as possible
ifftu_shifted=[ifftu(611:end,:);ifftu(1:610,:)];
clear ifftu

% Apply R0^(3/2) range weighting
ifftu_sh_rw=(R0.^(1.5)*ones(1,360)).*ifftu_shifted+eps;
clear ifftu_shifted
% Should I shift back before fft'ing?
% time (range) delay transforms to a phase shift...

Uprime=1/pi/sqrt(1.915)*fft(ifftu_sh_rw,[],1);
clear ifftu_sh_rw

%Find FF RCS
D=24*.0254; %diam (m) of circle that encloses bar & concentric w/meas
circ
N=ceil(max(k)*D)+10;

sumterm=zeros(701,360); %initialize sumterm
for n=-N:N
    sumterm=sumterm+...
        (-j)^n*(ones(701,1)*exp(-j*n*azrad))./... %(-j)^n * e^(-jn phi)
term
        ((sqrt(1./(1.915*pi*k)).*...
        exp(-j*(3.830*k-n*pi/2-pi/4)))*ones(1,360)).*... %H_n^(2)(pi k
rho0)
        ifft(Uprime,[],2); %integration term
end

S_FF=(2*sqrt(1.915./(j*pi*k))*ones(1,360)).*sumterm;

%Generate Plot
plot(az,20*log10(abs(4*pi*S_FF(351,:))),'k')
grid on
axis([0 360 -50 10])
set(gca,'xtick',[0 30 60 90 120 150 180 210 240 270 300 330 360])
xlabel('\phi (deg)')
ylabel('RCS (dBsm)')
%title('RCS Predicted by CNFFFT at 10GHz (Obviously Not Correctly
Implemented)')
set(gcf,'paperposition',[0.25 4 6 3.5])
% END OF CODE ----------------------------------------------------------
```

```
% loadcaldata.m
%-------------------------------------------------------
% This function loads the calibration data for the target
%-------------------------------------------------------

clear;clc;

load sphnew_tar.txt
load sphnew_bkg.txt
load cyl450_tar.txt
load cyl450_bkg.txt
load cyl450_6_14_vv_exact
load sph6in_6_14_exact

f=linspace(6e9,14e9,801).';

sph6in_tariq=complex(sphnew_tar(3:end,3),sphnew_tar(3:end,4));
sph6in_bkgiq=complex(sphnew_bkg(3:end,3),sphnew_bkg(3:end,4));
cyl450_tariq=complex(cyl450_tar(3:end,3),cyl450_tar(3:end,4));
cyl450_bkgiq=complex(cyl450_bkg(3:end,3),cyl450_bkg(3:end,4));

sph6in_subiq=sph6in_tariq-sph6in_bkgiq;
cyl450_subiq=cyl450_tariq-cyl450_bkgiq;

clear sphnew_tar sphnew_bkg
clear cyl450_tar cyl450_bkg
clear sph6in_tariq sph6in_bkgiq cyl450_tariq cyl450_bkgiq

save caldata
% END OF CODE ----------------------------------------------


% makeiq.m
%-------------------------------------------------------------
% This script creates the iq matrix from the raw ASCII data
%-------------------------------------------------------------

clear;clc;close all hidden;

% Load the Target Measurements
load bar_tar_ASCII

fmin=bar_tar(1,1)*1e9; %f_min (Hz)
fmax=bar_tar(1,2)*1e9; %f_max (Hz)
nf=bar_tar(1,3); %number of freq pts
azmax=bar_tar(2,1); %az max (deg)
azmin=bar_tar(2,2); %az min (deg)
naz=bar_tar(2,3); %number of az pts

% initialize I & Q matrices
I=zeros(nf,naz);
Q=zeros(nf,naz);

% fill I & Q matrices
```

```
for col=1:naz
    r1=(col-1)*nf+3; %start row for current az position
    r2=col*nf+2; %end row for current az position
    I(:,col)=bar_tar(r1:r2,3); %create a column of I data
    Q(:,col)=bar_tar(r1:r2,4); %create a column of Q data
end

tariq=complex(I,Q); %assemble I and Q matrices into one complex matrix

clear I Q r1 r2 col bar_tar

% Repeat Everything for the Background Measurements
load bar_bkg_ASCII

% initialize I & Q matrices
I=zeros(nf,naz);
Q=zeros(nf,naz);

% fill I & Q matrices
for col=1:naz
    r1=(col-1)*nf+3; %start row for current az position
    r2=col*nf+2; %end row for current az position
    I(:,col)=bar_bkg(r1:r2,3); %create a column of I data
    Q(:,col)=bar_bkg(r1:r2,4); %create a column of Q data
end

bkgiq=complex(I,Q); %assemble I and Q matrices into one complex matrix

bar_subiq=tariq-bkgiq;

clear tariq bkgiq
clear I Q r1 r2 col bar_bkg

save bar_data
% END OF CODE ------------------------------------------------------


% calbardata.m
%----------------------------------------------------------
% Calibrates the measured 2ft-bar data
%----------------------------------------------------------

clear;clc;close all hidden;

load bar_data
load caldata

t=linspace(0,1/(f(2)-f(1)),801).';

win=hamming(801); %window function
tg=blackman(41); %roll-off portion of time gate
gate=[zeros(203,1);tg(1:21);ones(19,1);tg(21:41);zeros(537,1)]; %gate
function

% Window and Timegate Measured Calibration Data
```

```
cyl450_subiq_td=ifft(win.*cyl450_subiq,[],1);
cyl450_subiq_g_td=gate.*cyl450_subiq_td;
cyl450_subiq_g=fft(cyl450_subiq_g_td,[],1);
sph6in_subiq_td=ifft(win.*sph6in_subiq,[],1);
sph6in_subiq_g_td=gate.*sph6in_subiq_td;
sph6in_subiq_g=fft(sph6in_subiq_g_td,[],1);

clear cyl450_subiq cyl450_subiq_td cyl450_subiq_g_td
clear sph6in_subiq sph6in_subiq_td sph6in_subiq_g_td

% Window and Timegate Measured Data from 2ft Bar
bar_subiq_td=ifft((win*ones(1,360)).*bar_subiq,[],1);
clear bar_subiq; %free memory
bar_subiq_g_td=(gate*ones(1,360)).*bar_subiq_td;
clear bar_subiq_td; %free memory
bar_subiq_g=fft(bar_subiq_g_td,[],1);
clear bar_subiq_g_td; %free memory

% Calibrate
caltarget=1; % cal with sphere (set to 0) or cylinder (set to 1)
if caltarget==0
    % Calibrate with 6 inch Sphere
    bar_g_cal=(sph6in_6_14_exact*ones(1,360)).*(bar_subiq_g)./...
        (sph6in_subiq_g*ones(1,360));
elseif caltarget==1
    % Calibrate with 4.5 inch Cylinder
    bar_g_cal=(cyl450_6_14_vv_exact*ones(1,360)).*(bar_subiq_g)./...
        (cyl450_subiq_g*ones(1,360));
else end

save bar_calibrated bar_g_cal
% END OF CODE ------------------------------------------------


% dualcal.m
%-------------------------------------------------------------
% This script performs a dual calibration on the calibration
% measurements taken for the 2-foot bar measurements and makes
% plots.  Averaging here was set to 1024 samples.
%-------------------------------------------------------------

clear;clc;close all hidden;

load sphnew_tar.txt
load sphnew_bkg.txt
load cyl450_tar.txt
load cyl450_bkg.txt

f=linspace(6e9,14e9,801).';

sph6in_6_14_tariq=complex(sphnew_tar(3:end,3),sphnew_tar(3:end,4));
sph6in_6_14_bkgiq=complex(sphnew_bkg(3:end,3),sphnew_bkg(3:end,4));
cyl450_6_14_tariq=complex(cyl450_tar(3:end,3),cyl450_tar(3:end,4));
cyl450_6_14_bkgiq=complex(cyl450_bkg(3:end,3),cyl450_bkg(3:end,4));
```

```
clear sphnew_tar sphnew_bkg
clear cyl450_tar cyl450_bkg

load cyl450_6_14_vv_exact
load sph6in_6_14_exact

t=linspace(0,1/(f(2)-f(1)),801).';

win=hamming(801);
tg=blackman(41);
gate=[zeros(203,1);tg(1:21);ones(19,1);tg(21:41);zeros(537,1)]; %gate
function

cyl450_6_14_subiq=cyl450_6_14_tariq-cyl450_6_14_bkgiq;
cyl450_6_14_subiq_td=ifft(win.*cyl450_6_14_subiq);
cyl450_6_14_subiq_g_td=gate.*cyl450_6_14_subiq_td;
cyl450_6_14_subiq_g=fft(cyl450_6_14_subiq_g_td);

sph6in_6_14_subiq=sph6in_6_14_tariq-sph6in_6_14_bkgiq;
sph6in_6_14_subiq_td=ifft(win.*sph6in_6_14_subiq);
sph6in_6_14_subiq_g_td=gate.*sph6in_6_14_subiq_td;
sph6in_6_14_subiq_g=fft(sph6in_6_14_subiq_g_td);

cyl450_6_14_g_cal=sph6in_6_14_exact.*(cyl450_6_14_subiq_g)./...
    (sph6in_6_14_subiq_g); % calibrate the cylinder with the sphere
sph6in_6_14_g_cal=cyl450_6_14_vv_exact.*(sph6in_6_14_subiq_g)./...
    (cyl450_6_14_subiq_g); % calibrate the sphere with the cylinder

figure
plot(f/1e9,20*log10(abs(cyl450_6_14_g_cal)),'k'),grid on,hold on
plot(f/1e9,20*log10(abs(cyl450_6_14_vv_exact)),'k:')
xlabel('freq (GHz)'),ylabel('RCS (dBsm)')
%title('Cyl RCS (Cal w/ Sph) vs. MoM/Exact Cyl RCS (BW=8GHz), Max Avg &
Sweep Time')
legend('Calibrated','MoM/Exact',0)
axis([6 14 -18 -12])
set(gcf,'paperposition',[0.25 4 6 3.5])

figure
plot(f/1e9,20*log10(abs(sph6in_6_14_g_cal)),'k'),grid on,hold on
plot(f/1e9,20*log10(abs(sph6in_6_14_exact)),'k:')
xlabel('freq (GHz)'),ylabel('RCS (dBsm)')
%title('Sph RCS (Cal w/ Cyl) vs. Exact Sph RCS (BW=8GHz), Max Avg &
Sweep Time')
legend('Calibrated','Exact',0)
axis([6 14 -19 -16])
set(gcf,'paperposition',[0.25 4 6 3.5])

dualcalerror=abs(20*log10(abs(sph6in_6_14_g_cal))-
20*log10(abs(sph6in_6_14_exact)));

figure
plot(f/1e9,dualcalerror,'k'),grid on
xlabel('freq (GHz)'),ylabel('error (dB)')
%title('Error Between Measured (Dual-Cal) and Exact RCS')
```

```
%legend('Calibrated','Exact',0)
axis([6 14 0 0.8])
set(gcf,'paperposition',[0.25 4 6 3.5])
% END OF CODE ------------------------------------------------


% bkgchar.m
%-------------------------------------------------------------
% This script generates a plot for background characterization
% of the 2-foot bar data.  Averaging was 1024 samples.
%-------------------------------------------------------------

clear;clc;close all hidden;

load sph6in_bkg.txt
load sph6in_bkg2.txt
load sph6in_bkg3.txt
load cyl450_bkg.txt
load cyl450_tar.txt

f=linspace(6e9,14e9,801).';

bkgiq1=complex(sph6in_bkg(3:end,3),sph6in_bkg(3:end,4));
bkgiq2=complex(sph6in_bkg2(3:end,3),sph6in_bkg2(3:end,4));
bkgiq3=complex(sph6in_bkg3(3:end,3),sph6in_bkg3(3:end,4));
bkgiq4=complex(cyl450_bkg(3:end,3),cyl450_bkg(3:end,4));
tariq=complex(cyl450_tar(3:end,3),cyl450_tar(3:end,4));
clear sph6in_bkg sph6in_bkg2 sph6in_bkg3
clear cyl450_bkg cyl450_tar

b21=bkgiq2-bkgiq1+eps; %bkg2 - bkg1
b31=bkgiq3-bkgiq1+eps; %bkg2 - bkg1
b41=bkgiq4-bkgiq1+eps; %bkg2 - bkg1
subiq=tariq-bkgiq4; %tar - bkg4 (cyl - cyl's bkg)

figure
plot(f/1e9,20*log10(abs(subiq)),'k',...
     f/1e9,20*log10(abs(b21)),'k:')
axis([6 14 -100 -50])
xlabel('f (GHz)')
ylabel('Magnitude of S_{11} (dB)')
%title('Calibration Cylinder & Bkg_2-Bkg_1')
grid on
legend('Cylinder','Bkg_2-Bkg_1')
set(gcf,'paperposition',[0.25 4 6 4.5])
% END OF CODE ------------------------------------------------


% figs_nfrcs.m
%-------------------------------------------------------------
% This script generates the figures for Near Field RCS
%-------------------------------------------------------------

clear;clc;close all hidden;
```

```
load bar_calibrated

u=bar_g_cal(51:751,:); %discard endpoints, keep 6.5GHz-13.5GHz
clear bar_g_cal
az=linspace(0,359,360);

figure
plot(az,20*log10(abs(u(351,:))),'k')
grid on
axis([0 360 -40 0])
xlabel('Azimuth Angle (deg)')
ylabel('RCS (dBsm)')
set(gca,'xtick',[0 30 60 90 120 150 180 210 240 270 300 330 360])
%title('Near Field RCS at 10GHz')
set(gcf,'paperposition',[0.25 4 6 3.5])

figure
plot(az,20*log10(abs(u(1,:))),'k')
grid on
axis([0 360 -40 0])
xlabel('Azimuth Angle (deg)')
ylabel('RCS (dBsm)')
set(gca,'xtick',[0 30 60 90 120 150 180 210 240 270 300 330 360])
%title('Near Field RCS at 6.5GHz')
set(gcf,'paperposition',[0.25 4 6 3.5])

figure
plot(az,20*log10(abs(u(701,:))),'k')
grid on
axis([0 360 -40 0])
xlabel('Azimuth Angle (deg)')
ylabel('RCS (dBsm)')
set(gca,'xtick',[0 30 60 90 120 150 180 210 240 270 300 330 360])
%title('Near Field RCS at 13.5GHz')
set(gcf,'paperposition',[0.25 4 6 3.5])
% END OF CODE ------------------------------------------------


% figs_phase.m
%-----------------------------------------------------------
% This program generates the phase plots for the NF data
%-----------------------------------------------------------

clear;clc;close all hidden;

load bar_calibrated

u=bar_g_cal(51:751,:); %discard endpoints, keep 6.5GHz-13.5GHz
clear bar_g_cal
az=linspace(0,359,360);

figure
plot(az,unwrap(angle(u(351,:))),'k')
grid on
axis([0 360 -10 120])
```

```
xlabel('Azimuth Angle (deg)')
ylabel('Phase Angle (radians)')
set(gca,'xtick',[0 30 60 90 120 150 180 210 240 270 300 330 360])
%title('Phase Data at 10GHz')
set(gcf,'paperposition',[0.25 4 6 3.5])

figure
plot(az,unwrap(angle(u(1,:))),'k')
grid on
axis([0 360 -10 120])
xlabel('Azimuth Angle (deg)')
ylabel('Phase Angle (radians)')
set(gca,'xtick',[0 30 60 90 120 150 180 210 240 270 300 330 360])
%title('Phase Data at 6.5GHz')
set(gcf,'paperposition',[0.25 4 6 3.5])

figure
plot(az,unwrap(angle(u(701,:))),'k')
grid on
axis([0 360 -10 120])
xlabel('Azimuth Angle (deg)')
ylabel('Phase Angle (radians)')
set(gca,'xtick',[0 30 60 90 120 150 180 210 240 270 300 330 360])
%title('Phase Data at 13.5GHz')
set(gcf,'paperposition',[0.25 4 6 3.5])
% END OF CODE -----------------------------------------------


% figs_xpatch.m
%-------------------------------------------------------------
% This script reads the data output from X-Patch and
% generates figures from that data.
%-------------------------------------------------------------

clear;clc;close all hidden;

load bar_10.txt
load bar_6.txt
load bar_14.txt

az=bar_10(:,2);
rcs_fcenter=bar_10(:,4);
rcs_fmin=bar_6(:,4);
rcs_fmax=bar_14(:,4);

figure,plot(az,rcs_fcenter,'k'),grid on
xlabel('\phi (deg)'),ylabel('RCS (dBsm)')
%title('X-Patch RCS of 2-foot cylinder at 10 GHz')
axis([0 360 -50 10])
set(gca,'xtick',[0 30 60 90 120 150 180 210 240 270 300 330 360])
set(gcf,'paperposition',[0.25 4 6 3.5])

figure,plot(az,rcs_fmin,'k'),grid on
xlabel('\phi (deg)'),ylabel('RCS (dBsm)')
%title('X-Patch RCS of 2-foot cylinder at 6.5 GHz')
```

```
axis([0 360 -50 10])
set(gca,'xtick',[0 30 60 90 120 150 180 210 240 270 300 330 360])
set(gcf,'paperposition',[0.25 4 6 3.5])

figure,plot(az,rcs_fmax,'k'),grid on
xlabel('\phi (deg)'),ylabel('RCS (dBsm)')
%title('X-Patch RCS of 2-foot cylinder at 13.5 GHz')
axis([0 360 -50 10])
set(gca,'xtick',[0 30 60 90 120 150 180 210 240 270 300 330 360])
set(gcf,'paperposition',[0.25 4 6 3.5])
% END OF CODE ------------------------------------------------
```

Appendix B: Additional Figures

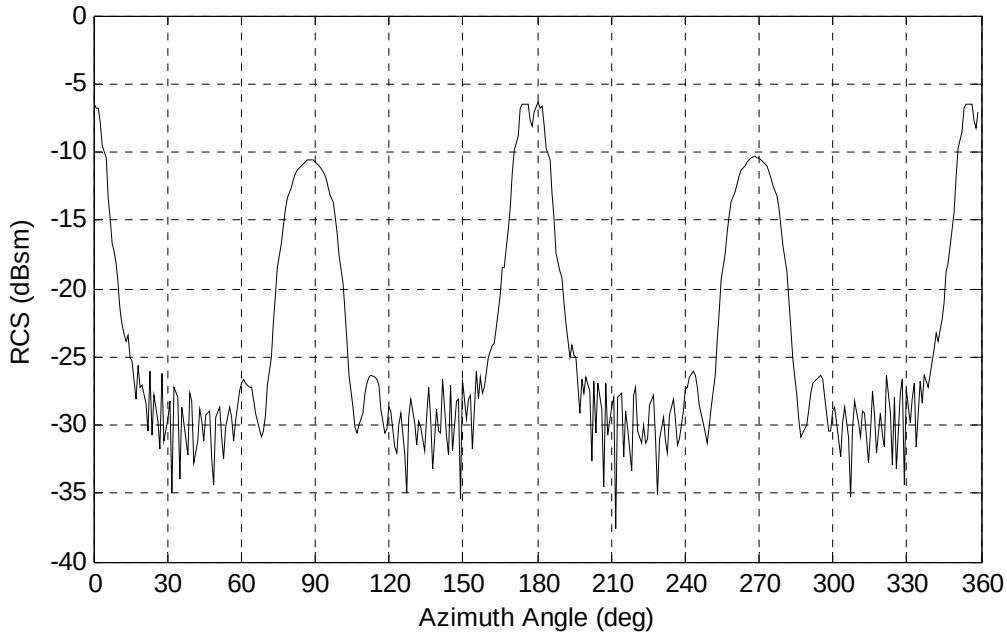

Figure 25. Near field RCS of 2-foot cylinder, v-pol, 6.5 GHz.

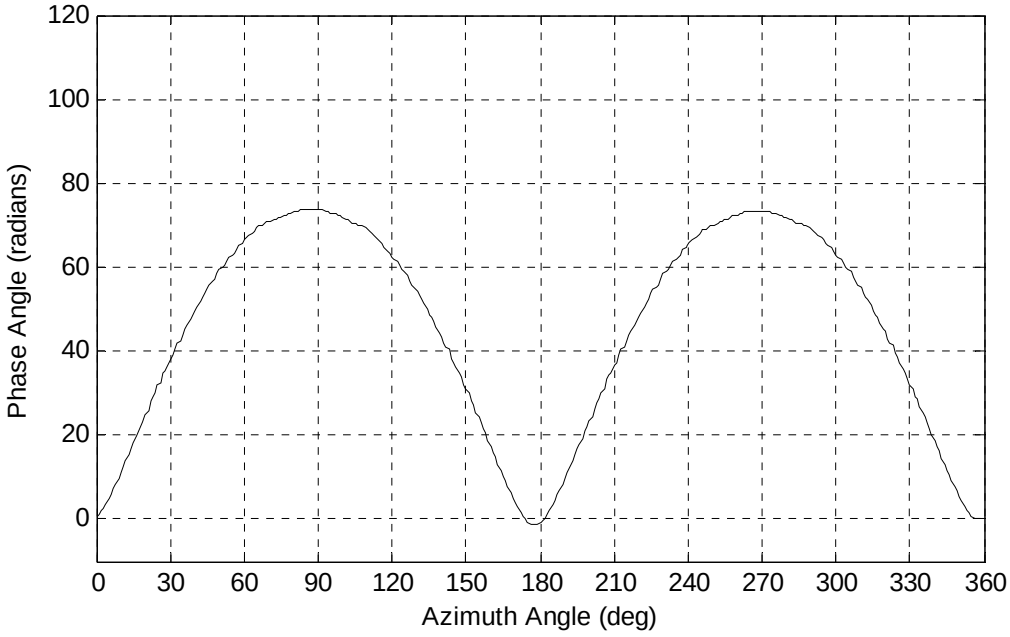

Figure 26. Near field phase data of 2-foot cylinder, v-pol, 6.5 GHz.

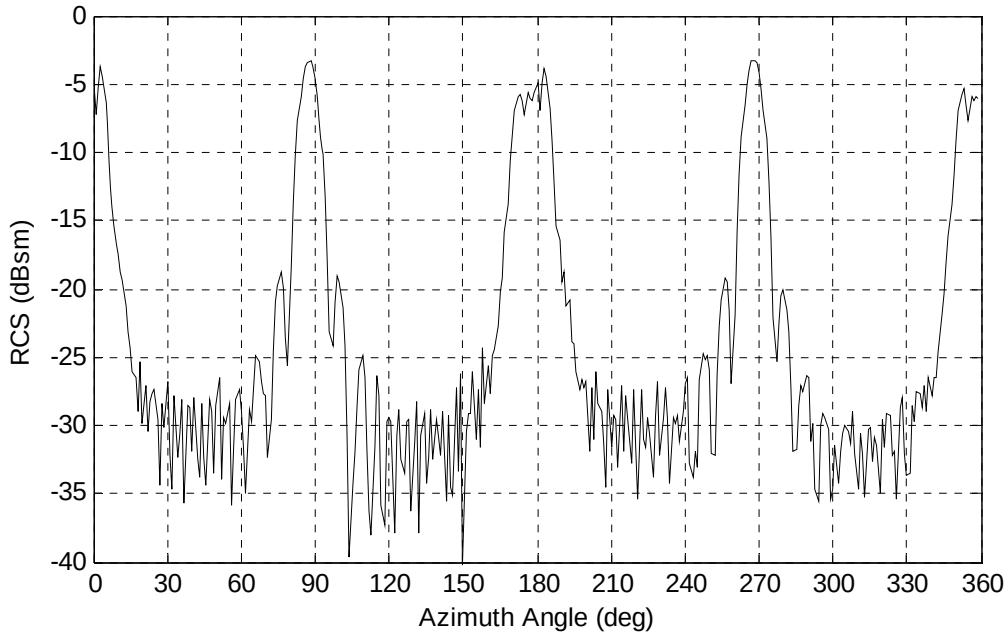

Figure 27. Near field RCS of 2-foot cylinder, v-pol, 13.5 GHz.

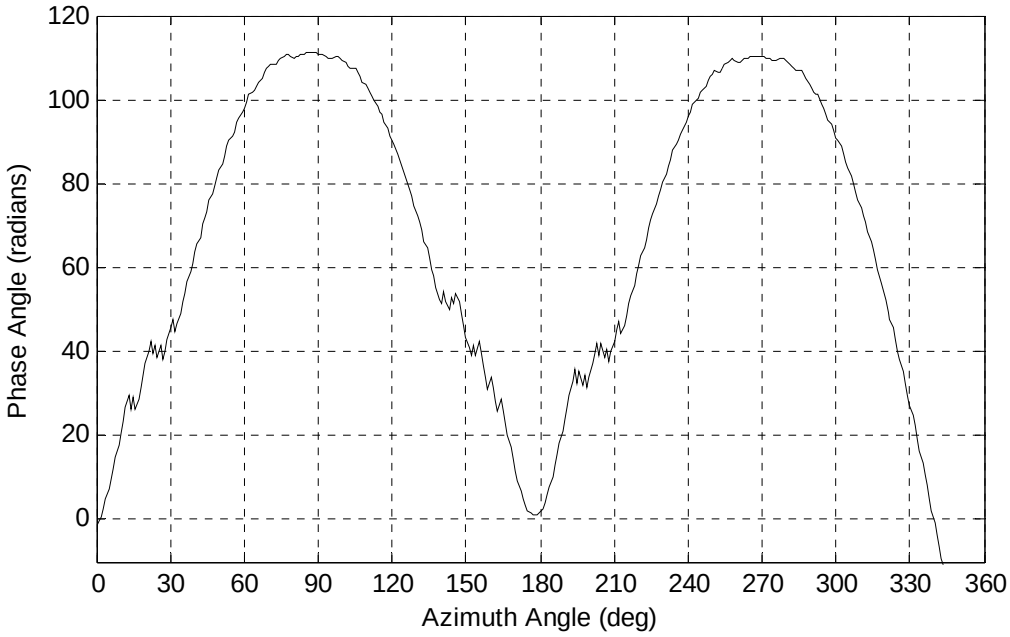

Figure 28. Near field phase data of 2-foot cylinder, v-pol, 13.5 GHz.

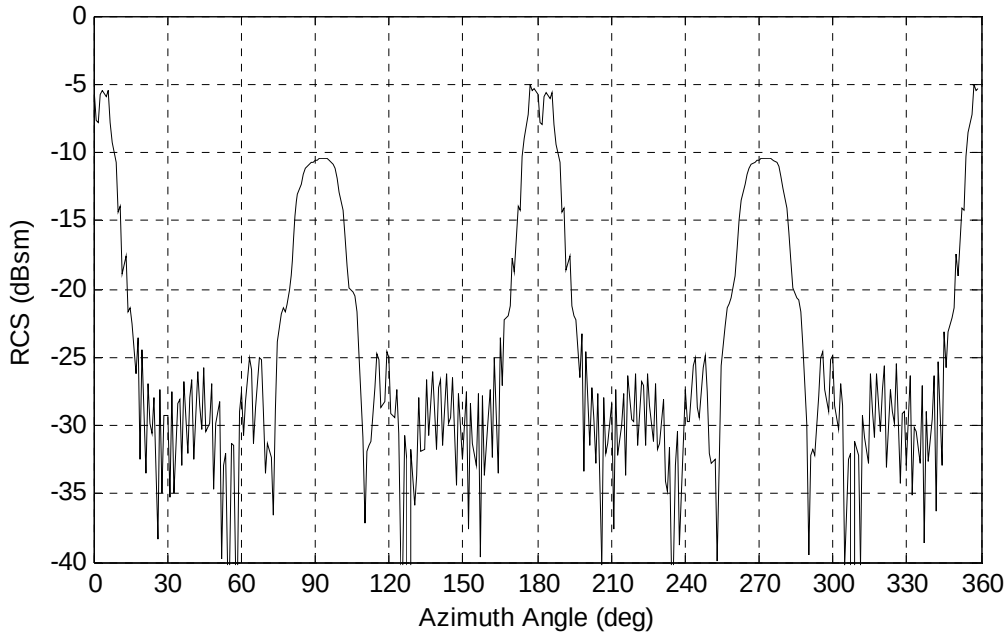

Figure 29. Near field RCS of 2-foot cylinder, h-pol, 6.5 GHz.

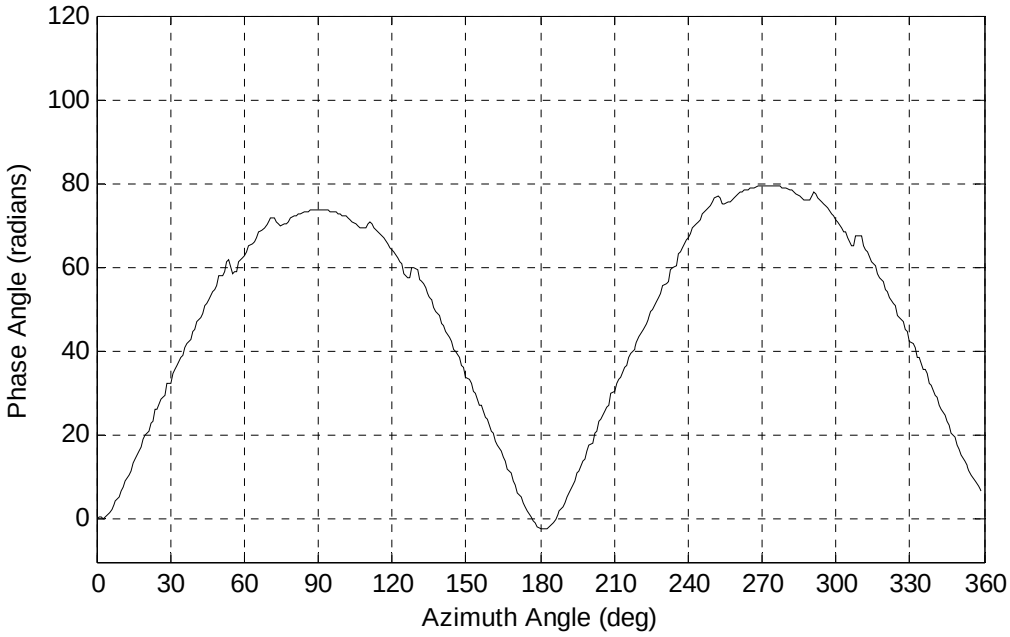

Figure 30. Near field phase data of 2-foot cylinder, h-pol, 6.5 GHz.

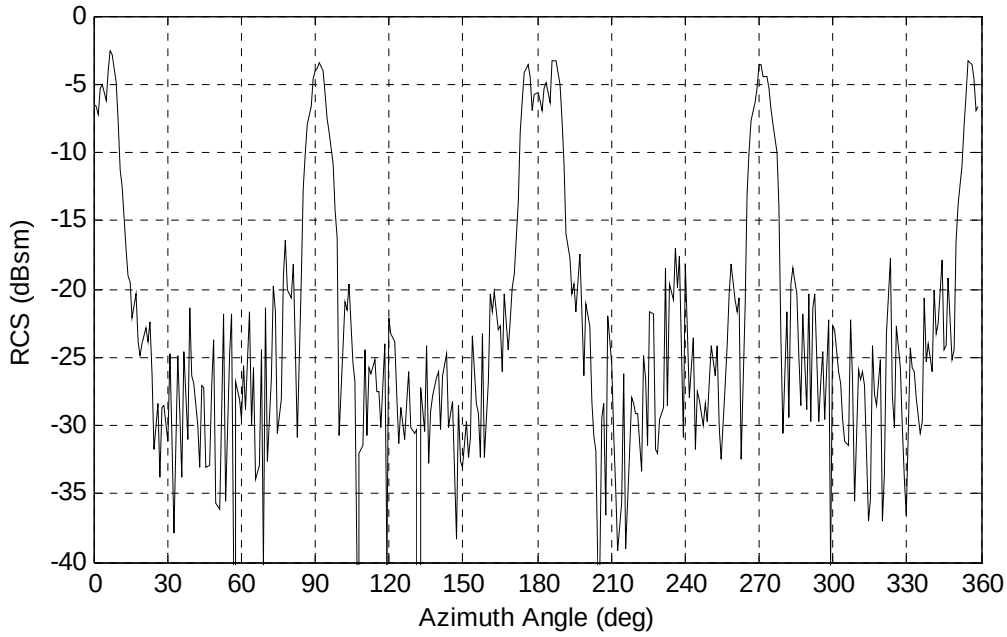

Figure 31. Near field RCS of 2-foot cylinder, h-pol, 13.5 GHz.

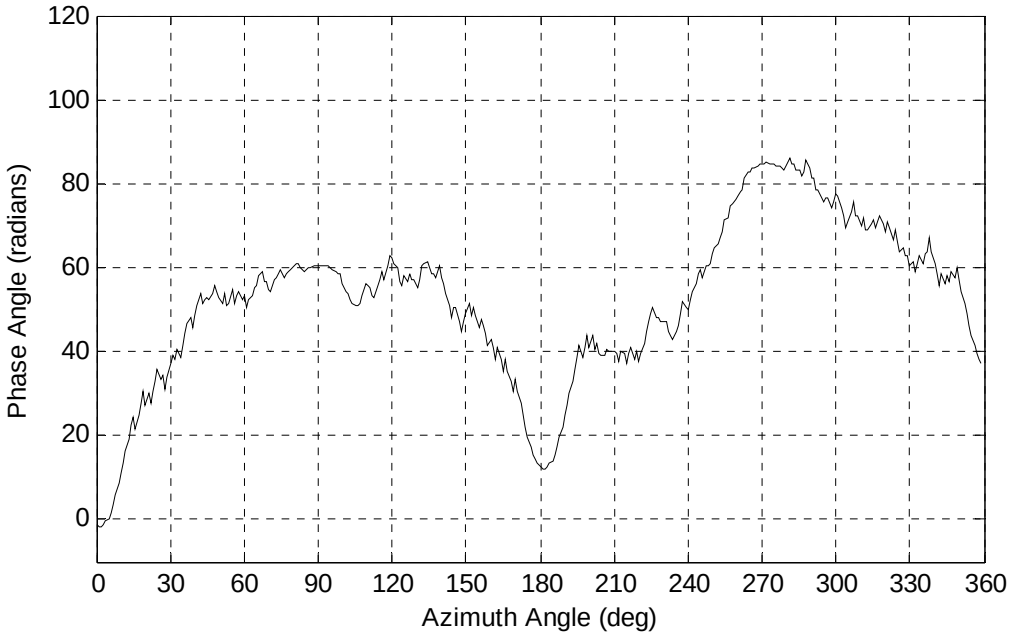

Figure 32. Near field phase data of 2-foot cylinder, h-pol, 13.5 GHz.

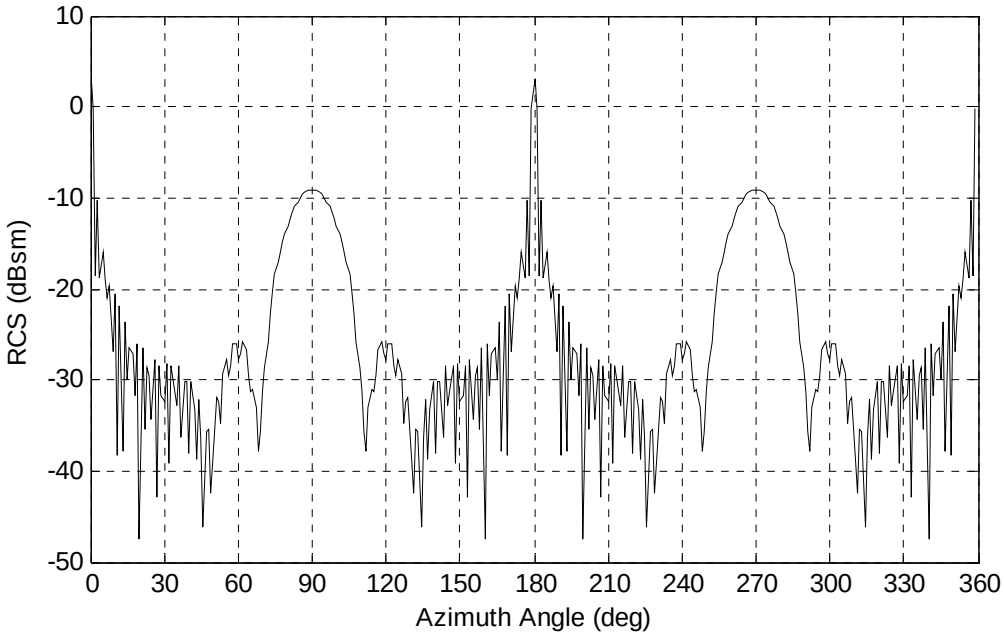

Figure 33. X-Patch far field RCS of 2-foot cylinder , 6.5 GHz.

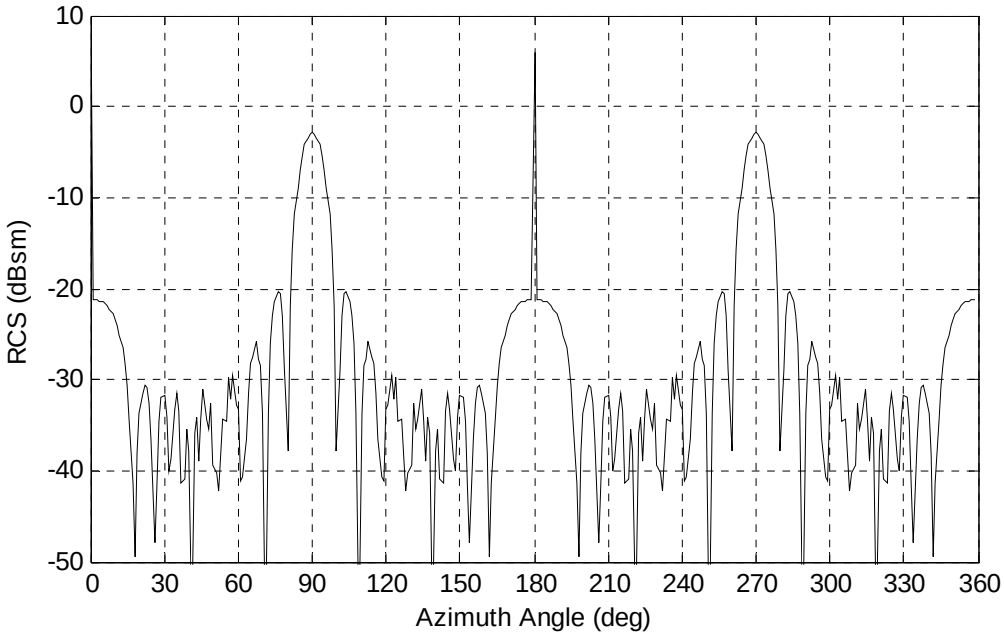

Figure 34. X-patch far field RCS of 2-foot cylinder, 13.5 GHz.

Bibliography

Balanis, Constantine A., *Antenna Theory: Analysis & Design, 3rd ed.*, Wiley, New York, 2005.

Balanis, Constantine A., *Advanced Engineering Electromagnetics,* Wiley, New York, 1989.

Falconer, David G., "Extrapolation of Near-Field Measurements to the Far Zone," *IEEE Transactions on Antennas and Propagation*, Vol. 36, No. 6, June, 1988.

Fischer, Brian E., et al., "On the Use of Wavenumber Migration for Linear SAR Image Formation and Near-Field to Far-Field RCS Transformation," *Proc. Of the 23rd Annual Meeting of the Antenna Measurement Techniques Association (AMTA '01)*, Denver, CO, 2001.

Kamen, Edward W. and Bonnie S. Heck, *Signals and Systems, 2nd ed.*, Prentice-Hall, New Jersey, 2000.

Knott, Eugene F., John F. Shaeffer, and Michael T. Tuley, *Radar Cross Section, 2nd ed.*, SciTech, Raleigh, NC, 2004.

LaHaie, Ivan J. and Scott A. Rice, "Antenna Pattern Correction for Near Field-to-Far Field RCS Transformation of 1-D Linear SAR Measurements," *Proc. Of the 25th Annual Meeting of the Antenna Measurement Techniques Association (AMTA '03)*, Irvine, CA, 2003.

LaHaie, Ivan J., "Overview of an Image-Based Technique for Predicting Far Field Radar Cross-Section from Near Field Measurements," *IEEE Antennas and Propagation Magazine*, Vol. 45, No. 6, pp. 159-169, December 2003.

LaHaie, Ivan J., Christopher M. Coleman, and Scott A Rice., "An Improved Version of the Circular Near Field-to-Far Field Transformation (CNFFFT)," *Proc. Of the 27th Annual Meeting of the Antenna Measurement Techniques Association (AMTA '05)*, Newport, RI, 2005.

Odendaal, J.W. and J. Joubert, "Radar Cross Section Measurements Using Near-Field Radar Imaging," *IEEE Transactions on Instrumentation and Measurement*, Vol. 45, No. 6, December, 1996.

Yaghjian, Arthur D., "An Overview of Near-Field Antenna Measurements," *IEEE Transactions on Antennas and Propagation*, Vol. AP-34, No. 1, January, 1986.

REPORT DOCUMENTATION PAGE

Form Approved
OMB No. 074-0188

The public reporting burden for this collection of information is estimated to average 1 hour per response, including the time for reviewing instructions, searching existing data sources, gathering and maintaining the data needed, and completing and reviewing the collection of information. Send comments regarding this burden estimate or any other aspect of the collection of information, including suggestions for reducing this burden to Department of Defense, Washington Headquarters Services, Directorate for Information Operations and Reports (0704-0188), 1215 Jefferson Davis Highway, Suite 1204, Arlington, VA 22202-4302. Respondents should be aware that notwithstanding any other provision of law, no person shall be subject to an penalty for failing to comply with a collection of information if it does not display a currently valid OMB control number.
PLEASE DO NOT RETURN YOUR FORM TO THE ABOVE ADDRESS.

1. REPORT DATE *(DD-MM-YYYY)*	**2. REPORT TYPE**	**3. DATES COVERED** *(From – To)*
23-03-2006	**Master's Thesis**	Sep 2004 – Mar 2006

4. TITLE AND SUBTITLE

A Study of Near Field Data Transformed to the Far Field for a Canonical PEC Scatterer

5a. CONTRACT NUMBER

5b. GRANT NUMBER

5c. PROGRAM ELEMENT NUMBER

6. AUTHOR(S)

E. Matthew Cady

5d. PROJECT NUMBER

5e. TASK NUMBER

5f. WORK UNIT NUMBER

7. PERFORMING ORGANIZATION NAMES(S) AND ADDRESS(S)
Air Force Institute of Technology
Graduate School of Engineering and Management (AFIT/EN)
2950 Hobson Way
WPAFB OH 45433-7765

8. PERFORMING ORGANIZATION REPORT NUMBER

AFIT/GE/ENG/06-11

9. SPONSORING/MONITORING AGENCY NAME(S) AND ADDRESS(ES)
ASC/ENAD
Attn: Dr. Frederick A. Tokarz
2530 Loop Road West, B560
WPAFB OH 45433-7101 DSN: 785-9286

10. SPONSOR/MONITOR'S ACRONYM(S)

11. SPONSOR/MONITOR'S REPORT NUMBER(S)

12. DISTRIBUTION/AVAILABILITY STATEMENT
APPROVED FOR PUBLIC RELEASE; DISTRIBUTION UNLIMITED.

13. SUPPLEMENTARY NOTES

14. ABSTRACT

The purpose of this research was to analyze the error associated with the Image Based Near Field to Far Field Transformation (IB NFFFT) for a canonical perfectly electrically conductive (PEC) scatterer. This research compares two groups of data: far field RCS predicted by the IB NFFFT and far field RCS predicted by X-Patch. The IB NFFFT requires a complete set of calibrated monostatic near field scattering data of the object. A detailed description is given of the configuration of the measurement facilities and procedures that were required to obtain the calibrated near field scattering data, as well as the process for implementing the transformation. Additional chamber characterization techniques are also presented. For this research, a 2-foot long aluminum cylinder of 3-inch diameter was used as the canonical scattering body.

15. SUBJECT TERMS

Radar cross sections, Near field, Far field, Electromagnetic scattering

16. SECURITY CLASSIFICATION OF:			**17. LIMITATION OF ABSTRACT**	**18. NUMBER OF PAGES**	**19a. NAME OF RESPONSIBLE PERSON**
REPORT	**ABSTRACT**	**c. THIS PAGE**			Andrew J. Terzuoli, PhD, (ENG)
U	**U**	**U**	**UU**	95	**19b. TELEPHONE NUMBER** *(Include area code)* (937) 255-3636, ext 4717; e-mail: Andrew.Terzuoli@afit.edu